1   Elastic anisotropies of deformed upper crustal rocks in the Alps

3   Ruth Keppler (1), Roman Vasin (2), Michael Stipp, (3), Tomás Lokajícek (4), Matej Petruzálek (4), Nikolaus
4   Froitzheim (1)

6   Corresponding author: Ruth Keppler (rkep@uni-bonn.de)

8   [1] Institute for Geosciences, University of Bonn, Poppelsdorfer Schloss, D-53115 Bonn, Germany
9   [2] Frank Laboratory of Neutron Physics, Joint Institute for Nuclear Research, Joliot-Curie 6, 141980 Dubna,
10 Russia
11 [3] Institute for Geosciences and Geography, Von-Seckendorff-Platz 3, D-06120 Halle (Saale), Germany
12 [4] Institute of Geology of the Czech Academy of Sciences, Rozvojova 269, 16000 Prague 6, Czech Republic

14
15 ABSTRACT

17 The upper crust within collisional orogens is very heterogeneous both in composition and grade of
18 deformation, leading to very variable physical properties at small scales. This yields difficulties for seismic
19 investigations of tectonic structures at depth since local changes in elastic anisotropy cannot be detected.
20 In this study, we show elastic anisotropies of the range of typical lithologies within deformed upper crustal
21 rocks in the Alps. Furthermore, we aim to model average elastic anisotropies for these rocks and their
22 changes with increasing depth due to the closure of microcracks. We therefore sampled rocks in the Adula
23 Nappe of the central Alps, which is typical for upper crust in collisional orogens. The two major rock types
24 found are orthogneisses and paragneisses, however, small lenses of metabasites and marbles also occur.
25 Crystallographic preferred orientations (CPOs) and volume fractions of minerals in the samples were
26 measured using time-of-flight neutron diffraction. Combined with single crystal elastic anisotropies these
27 were used to model seismic properties of the rocks. The sample set shows a wide range of different seismic
28 velocity patterns even within the same lithology, due to the heterogeneity of deformed upper crust. To
29 approximate an average for these upper crustal units, we picked common CPO types of rock forming
30 minerals within the gneiss samples, which represent the most common lithology. These data were used to
31 determine an average elastic anisotropy of a typical upper crustal rock within the Alps. Average mineral
32 volume percentages within the gneiss samples were used for the calculation. In addition, ultrasonic
33 measurements of elastic anisotropies of the samples at increasing pressures were performed. These
34 measurements, as well as the microcrack pattern determined in thin sections of the samples were used to
35 model the closure of microcracks in the average sample at increasing depth. At ≈740 MPa microcracks are
36 assumed to be closed yielding average elastic anisotropies of 4% for the average gneiss. This value is an
37 approximation, which can be helpful for seismic models at a lithospheric scale. At a crustal or smaller scale,
38 however, it is an oversimplification and local lithological as well as deformational changes shown by the
39 range of elastic anisotropies within the sample set have to be considered.

40
41
42

1. Introduction

Geophysical studies of the crust and mantle of the Earth are constantly improving and detailed investigations of structures at increasingly higher depth are possible. High-resolution geophysical imaging of 3D structures is currently taking place within the AlpArray initiative using a high-end seismological array in the Alpine orogen. For this as well as other similar projects around the world there is a demand for precise input parameters and knowledge of the physical properties of the rocks at depth. Especially elastic anisotropy data is of importance, since it reflects the plastic deformation of rocks. Rock elastic anisotropy at mantle depth is mainly caused by crystallographic preferred orientation (CPO) of the constituent mineral phases. At lower depth microcracks additionally influence elastic properties by both lowering seismic velocity and increasing the elastic anisotropy in deformed rocks. Elastic anisotropy data of rocks can be either be gained by measurements in high pressure vessels using ultrasound (e.g., Babuška, 1968; Kern and Wenk, 1990; Pros et al., 2003; Ivankina et al., 2005; Kern et al., 2008; Lokajicek et al., 2014; Vasin et al.,2017; Ullemeyer et al., 2018), or modeled using the CPO data of the constituent minerals and their corresponding single crystal elastic anisotropies (e.g. Mainprice and Humbert, 1994; Barruol and Kern, 1996; Mauler et al., 2000; Bascou et al., 2001; Ivankina et al., 2005; Kitamura, 2006; Kern et al., 2008; Abalos et al., 2010; Llana-Fúnez and Brown, 2012; Keppler et al., 2015; Almqvist and Mainprice, 2017). In experimental investigations, despite pressure vessels operating at up to 600 MPa during measurements, microcracks in rock samples are not completely closed (Christensen, 1974; Vasin et al., 2017), which is why the resulting data are only comparable to elastic anisotropies within normal crustal depth, whereas the modeled anisotropies yield results for a crack free medium at higher depths (e.g., within thickened crust or at mantle depth).

The problem using elastic anisotropy data of natural rocks as input parameters for seismic investigation is the difference in scale. There is a gap between the km-scale of detectable units in seismic imaging at depth and the centimeter-sized rock samples taken from outcrops of several meters in the field. This is not an issue in the relatively homogenous mantle with a fairly simple mineralogy. Crustal rocks, however, are not only polymineralic but the lithologies are variable. Additionally, deformation is also heterogeneous within the crust. Especially subduction zones and collisional orogens show a complex deformational history (e.g., Schmid et al., 2004; Simancas et al., 2005; Zhang et al., 2012). This leads to a large variety of different CPO patterns throughout a km scale geological unit (Schmidtke et al. submitted to same issue). Averaging the calculated or measured elastic anisotropies may lead to the prediction of an unrealistically isotropic medium, for the more strongly deformed parts of the crust.

It is therefore essential to classify the crust according to its composition and grade of deformation to define larger units which can be summarized. Since only deformed parts of the crust exhibit elastic anisotropy, this study is focused on the Adula Nappe of the Central Alps, which is representative for upper crustal rocks deformed during the Alpine Orogeny. CPO as well as volume percentages of all mineral phases from a large set of samples of this unit were determined. Subsequently, elastic anisotropies of the samples were calculated. These show a wide range of seismic properties of deformed upper crustal rocks in the Alps. Most of the samples are gneisses, which represent the most common rock type in the Adula Nappe. Based on the characteristic CPO types, average CPO strengths and average volume percentages of the relevant mineral phases, we calculated the elastic anisotropy of an "average rock", which represents an average anisotropy for deformed upper crustal rocks in collisional orogens. The two major lithologies are

85 orthogneisses and paragneisses, which is why the "average rock" has typical gneiss CPO and composition.
86 Furthermore, at shallow depth microcracks within the rocks are an important factor. Therefore, we used
87 data from ultrasonic measurements as well as thin section analysis to determine typical crack patterns in
88 the samples. From these the influence of microcracks on elastic properties was quantified, as well as the
89 changes in elastic anisotropy with increasing depth up to the point where all microcracks are presumably
90 closed.
91 This is, of course, a simplification of the very heterogeneous upper crust of the Alps, as already shown by
92 the variability of elastic anisotropy of the individual samples from the Adula Nappe. Yet, such an average
93 rock can be used for lithospheric and upper mantle scale seismic models, in which the crust is implemented
94 as a single unit with an average anisotropy. In crustal scale models the heterogeneity of different rocks
95 caused by variable composition as well as variable deformation have to be considered. While it is difficult
96 to present a universal average anisotropy for the very heterogeneous crust within collisional orogens, this
97 contribution represents a first approximation to close the scale gap between elastic anisotropy data of
98 rock samples and the kilometer scale structures measured in seismic investigations at greater depth.
99
100
101 2. Elastic anisotropies within the Alpine orogen
102
103 The Alpine Orogen exhibits a mountain-belt-parallel seismic anisotropy (e.g., Silver, 1996; Smith and
104 Ekström, 1999), which is not completely understood. In the Western Alps this anisotropy was illustrated
105 by teleseismic shear wave splitting and interpreted as a result of asthenospheric flow beneath the
106 lithospheric slab, although a further influence by lithospheric anisotropy due to Alpine deformation could
107 not be excluded (Barruol et al., 2004; 2011). Fry et al. (2010), on the other hand, determined seismic
108 anisotropies within the Alps by passive seismic imaging using Rayleigh wave phase velocities. Their results
109 suggest two distinct vertically distributed layers of anisotropy – an orogen-parallel fast direction down to
110 30 km and an orogen-perpendicular one between 30 and 70 km depth - with different geodynamic origins.
111 The authors interpret the orogen-parallel anisotropy as a consequence of CPO of crustal minerals (e.g.
112 amphibole and biotite) in response to compression and consider the deeper, orogen-perpendicular
113 anisotropy to result from bending and flow of the European lithospheric mantle.
114 The deep structure of the Western and Central Alps is mainly the result of subduction and collision
115 processes during the Paleogene and Neogene when the Penninic ocean basins were subducted and Adria,
116 Iberia, and other continental fragments collided with Europe. We consider a simplified version of the NFP-
117 20 EAST&EGT profile (Fig. 1A; Schmid and Kissling, 2000). We exclude nappe structures in the shallowest
118 part of the profile, like the Helvetic nappes. This results in a profile including the following upper crustal
119 units: the Aar and Gotthard massifs representing weakly deformed European basement; the Lucomagno,
120 Simano and Adula nappes of deformed European basement and Mesozoic cover; and relatively
121 undeformed Apulian upper crust. To simplify, we therefore subdivide the profile into
122
123 (1) weakly deformed isotropic upper crust
124
125 (2) strongly deformed anisotropic upper crust mostly comprising gneiss (Fig. 1B).
126
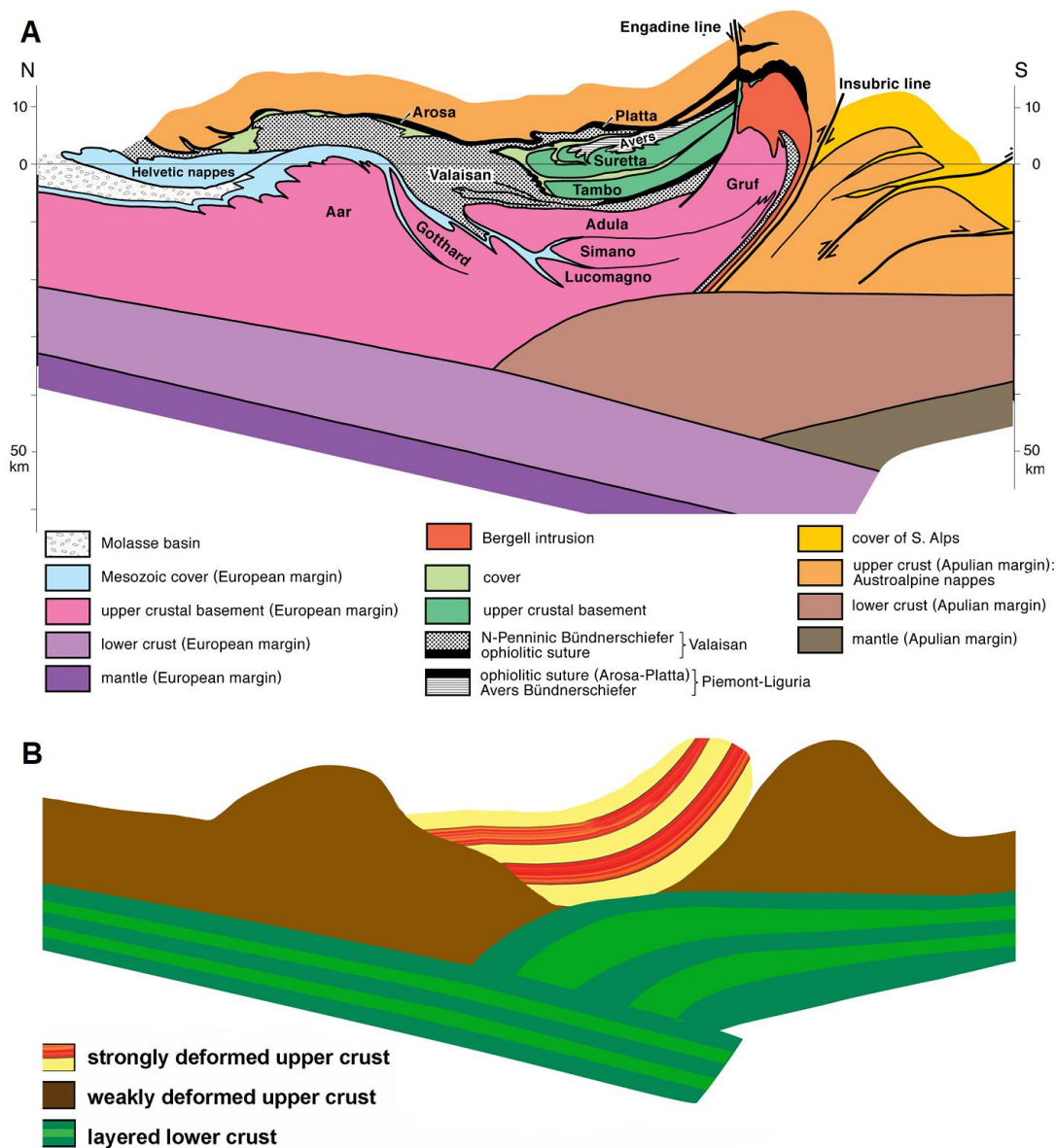
Figure 1: (A) North-south tectonic profile through the central Alps showing all major units (NFP-20 EAST&EGT; Schmid and Kissling, 2000) (B) strongly simplified profile through the same units, representing the predominant type of rock unit and neglecting the sedimentary cover and ophiolite units

2.1. Weakly deformed Alpine upper crust

In this study, both the crystalline massifs in the northern part of the central Alps and the Adriatic basement in the Southern Alps are assumed to show weak or no elastic anisotropy.

136   The Aar and Gotthard massifs contain large Variscan granitoid bodies which intruded into a pre-Variscan
137   basement. These units have only weakly been overprinted by Alpine metamorphism and deformation
138   (e.g., Abrecht, 1994; Schaltegger, 1994; Oliot et al., 2010). However, some greenschist to amphibolite
139   facies shear zones have been documented, which have to be considered for any large scale model
140   (Challandes et al., 2008; Goncalves et al., 2012; Wehrens et al., 2017).

141   In the Southern Alps, metamorphic grade during deformation was generally low. Deformation in the
142   basement is limited to large scale thrusting during Alpine tectonics (e.g., Laubscher 1985). For
143   simplification we are assuming an elastically isotropic medium for both the Variscan granitoids and the
144   southern Alps due to the lack of pervasive CPO forming deformation. One needs to bear in mind however,
145   that local ductile shear zones as well as large brittle faults also have an influence on the overall elastic
146   anisotropy (e.g. Almqvist et al., 2013).

147

148   2.2. Strongly deformed Alpine upper crust

149

150   As suggested by strong reflectors in the original NFP-20-east seismic profile (Pfiffner et al., 1988), as well
151   as numerous geological field studies, the crustal units in the central part (concerning their position in the
152   N-S running profile) of the central Alps have been strongly deformed during subduction and subsequent
153   continental collision (Fig. 1B).
154

155
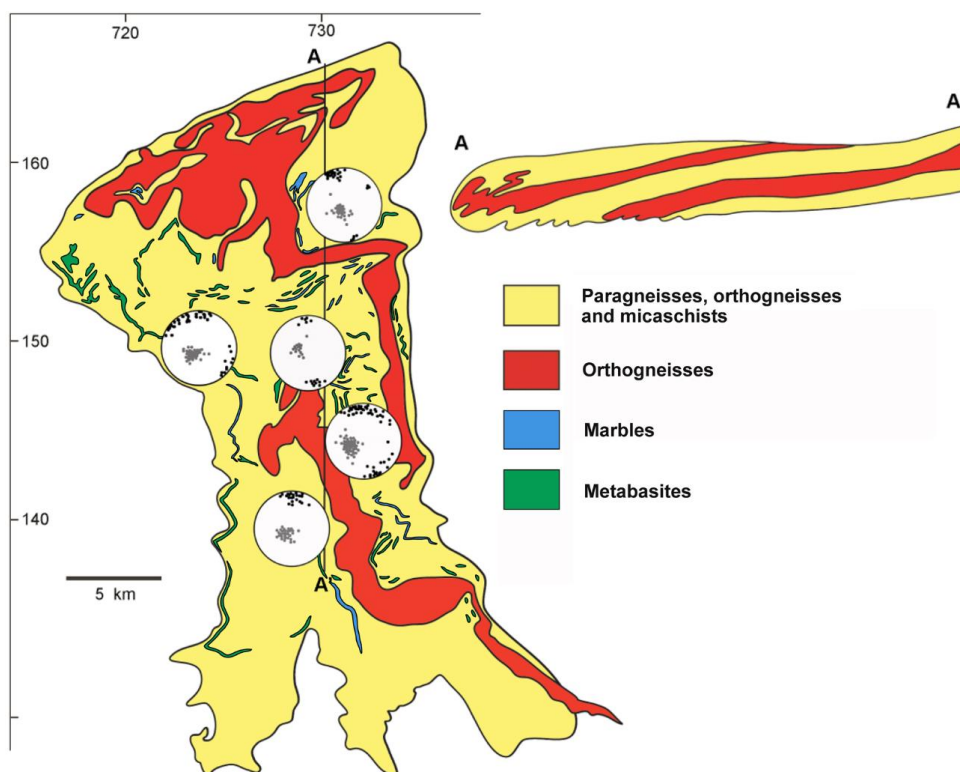
Figure 2: Simplified tectonic map and north-south profile of the Adula Nappe in the Swiss coordinate system (after Nagel. 2008). Grey and black dots indicate poles of main foliation and stretching lineation, respectively, in the central Adula Nappe.

The Adula Nappe together with the Simano and Lucomagno nappes constitutes the Lepontine dome, which mostly consists of Alpine nappes including Variscan basement and its Mesozoic cover. In this study, the Adula Nappe is taken as an example for the strongly deformed parts of the Alps. It represents a relatively coherent unit with stratigraphic basement-cover contacts. It was originally part of the distal European continental margin and entered a south-dipping subduction zone in which the Valais (North Peninnic) Ocean had been consumed. The unit shows peak conditions of 12–17 kbar/500–600 C° in the north and 30 kbar/800–850 C° in the south (e.g. Heinrich, 1986; Löw,1987; Meyre et al., 1997; Nagel et al. 2002; Dale and Holland, 2003). It mainly comprises orthogneisses and paragneisses with interlayers of schists, quartzites, marbles and metabasic lenses (Fig. 2). All lithologies were sampled, however most samples are orthogneisses and paragneisses, since these lithologies make up the largest part of the nappe and other lithologies might be too small scale to be detected in seismic imaging.

From peak conditions to its current position within the Lepontine dome, the Adula Nappe underwent several deformation phases. The oldest, peak to post-peak deformation phase is the eclogite facies Zapport phase, which is well documented in the central part of the nappe, where it was not overprinted by younger deformation phases (e.g. Löw, 1987; Meyre et al., 1993; Pleuger et al., 2003). Samples used for this study are from this area and represent deformed crustal parts of the Alps.

3. Methods

3.1. CPO analysis

CPO measurements were performed at the neutron time-of-flight (TOF) texture diffractometer SKAT at the Frank Laboratory of Neutron Physics at JINR, Dubna, Russia (Ullemeyer et al., 1998; Keppler et al., 2014). The high penetration capability of neutrons into matter together with the large beam cross section of the SKAT (50×95 mm^2) allow measurements of large-volume samples. In this study, roughly spherical samples with volumes of about 65 cm^3 were measured. Since the investigated samples are usually coarse-grained this guarantees good grain statistics. Moreover, since diffraction patterns are recorded in a TOF experiment over a large interval of lattice spacings, often containing hundreds of diffraction peaks, the so-called 'Rietveld Texture Analysis' can be used for the texture evaluation, allowing the simultaneous determination of all mineral textures even for samples with complex mineralogy (Von Dreele, 1997; Matthies et al. 1997), as well as defining the rock mineral composition. We used the MAUD software for the texture evaluation (Lutterotti et al., 1997; Wenk et al., 2010; Schmidtke et al., submitted to same issue). For every sample, a sample coordinate system XYZ representing the three directions of the finite strain ellipsoid was chosen. X is the lineation direction, Y is within the foliation plane perpendicular to the lineation and Z is the foliation normal.

3.2. Modeling of elastic anisotropies

From the orientation distribution function (ODF) of the main rock constituents, their volume fractions in each sample and particular single crystal elastic constants, the elastic moduli of bulk rock were calculated. For that purpose, simple averaging schemes are often used, such as Voigt approach (Voigt, 1887) or Reuss approach (Reuss, 1929). The former assumes that all crystallites in the polycrystal are under the same strain, while the latter considers equal stress state in all crystallites. To get a first approximation on the different elastic anisotropy patterns within the set of samples, we used the Voigt averaging scheme that provides reasonably good agreement of rock petrofabric data and laboratory measurements (Ben Ismail and Mainprice, 1998), while noting that the recalculated elastic properties represent the upper boundary of the polycrystal stiffness.

The single crystal elastic constants for the calculation were taken from the literature (muscovite: Vaughan and Guggenheim, 1986; quartz: Heyliger et al., 2003; albite: Brown et al., 2006; calcite: Dandekar, 1968; dolomite: Humbert & Plique, 1972; hornblende: Aleksandrov and Ryzhova, 1961; epidote: Aleksandrov et al., 1974; garnet: Zhang et al., 2008; omphacite: Bhagat et al., 1992).

Phase elastic wave velocities were calculated from bulk elastic tensors of rocks using the Christoffel equation.

To calculate the elastic anisotropy of the "average rock", representative of the upper crustal lithology, and its changes with overburden depth due to closure of the microcracks (see section 4.5), a more sophisticated approach to the calculation of rock elastic properties is necessary. We used a modified self-consistent method GeoMIXself (GMS; Matthies, 2010; 2012), which combines the standard self-consistent routines (e.g. Morris 1970) with elements of the geometric mean averaging (Matthies & Humbert 1995). This method is able to take CPO, morphologies and shape preferred orientations (SPOs) of grains, as well as pores and cracks, into account. Details and limitations of this approach for an application to polymineral rocks are discussed in, e.g., (Vasin et al., 2013; Vasin et al., 2017; Lokajicek et al., 2021).

3.3. Ultrasonic measurements

From the sample set, two samples with common CPO patterns and strengths of their constituent mineral phases were picked for ultrasonic measurements of P-wave velocity distributions at the pressure apparatus of the Institute of Geology ASCR, Prague, Czech Republic (e.g. Lokajicek et al., 2014). The measurements were conducted on spherical samples with diameters of 41.0 mm (RK15-17) and 39.4 mm (RK15-22), respectively. Before the measurement, the samples were dried at 100°C for 24 hours. Afterwards they were covered by a thin layer of epoxy resin to protect inner pore space of the sample against the hydrostatic pressure. Transformer oil served as the hydraulic medium. Ultrasonic signals were excited and recorded using a pair of piezoceramic sensors with a resonant frequency of 2 MHz. P-wave velocities were measured in 132 independent directions at differing confining pressure levels from ambient conditions to a maximum pressure of 300 or 400 MPa.

4. Results

4.1. Samples description

239   The orthogneiss samples consist of quartz, plagioclase, potassium feldspar and mica (Table 1A). Mica is
240   mostly white mica but a few samples also contain biotite. Mica is frequently aligned within the foliation
241   plane. It occurs in layers in some samples but exhibits single grains or clusters scattered within a matrix of
242   quartz and feldspar in most orthogneisses. Microcracks in mica grains are mostly aligned with its basal
243   plane, however there are also some mircocracks cutting across basal planes (Fig 3A-C). Quartz grains
244   exhibit signs of dynamic recrystallization.
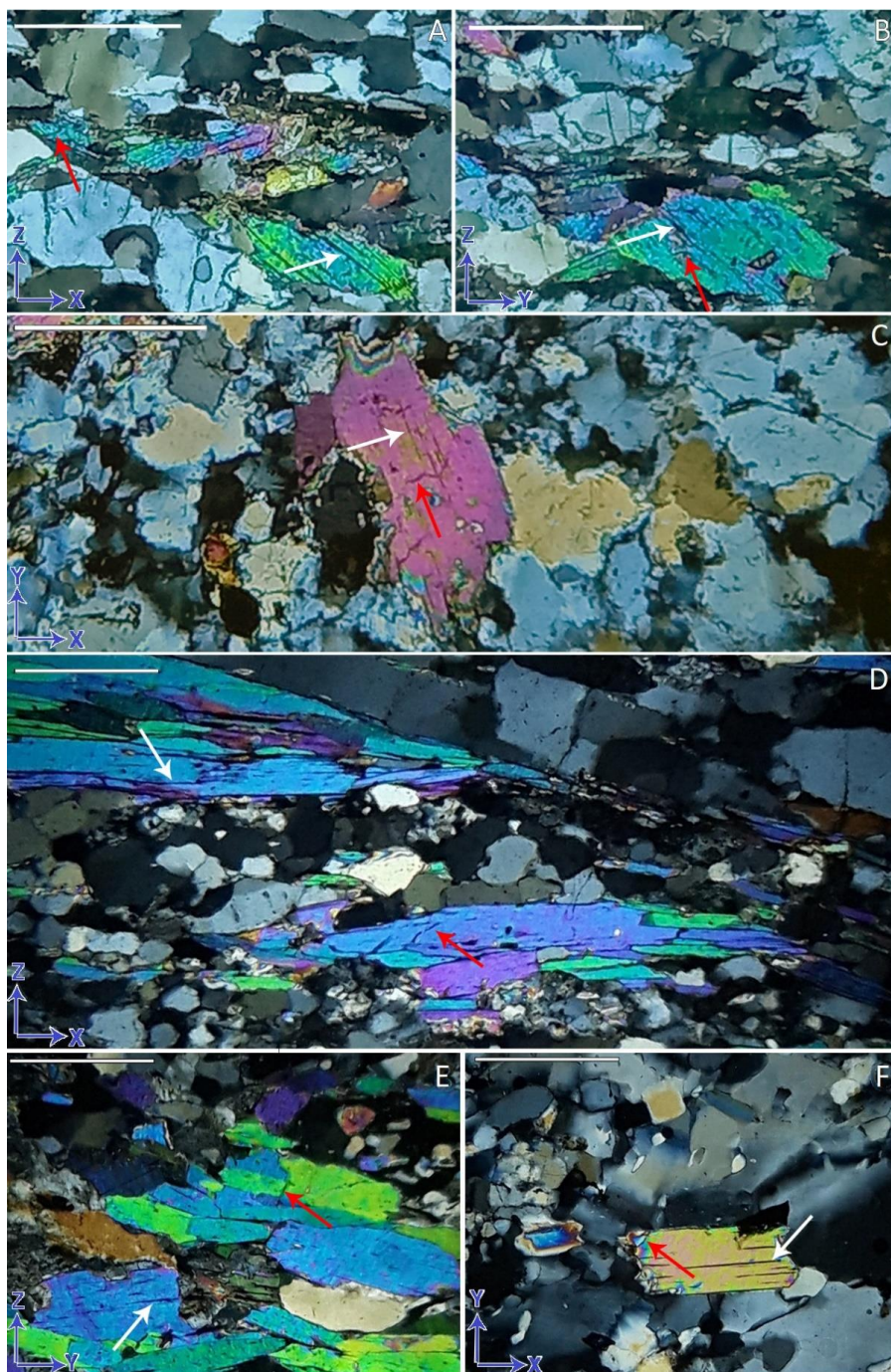
Figure 3: Thin sections of a typical orthogneiss (A, B, C) and paragneiss (D, E, F) under crossed polarizers
for the XZ (A, D), YZ (B, E) and XY plane (C, F), showing examples microcracks both parallel (white arrows)

245
246
247

248 and oblique (red arrows) to the mica basal planes. Blue arrows indicate the three directions of the finite
249 strain ellipsoid. White bar on upper left corner in each picture shows the length of 500 μm.

A	Composition in Volume %	Location	B	Composition in Volume %	Location
GAN12	48 Qz, 31 Plg, 21 Kfs	Alp de Ganan	GAN08	36 Qz, 23 Plg, 31 Mica, 10 Grt	Alp de Ganan
JK6	39 Qz, 43 Plg, 18 Mica	720 652/155 999	GAN15	45 Qz, 26 Plg, 29 Mica	Alp de Ganan
MS17-15	25 Qz, 32 Plg, 11 Kfs, 32 Mica	732 692/140 078	MS17-12B	51 Qz, 20 Plg, 29 Mica	734 127/140 223
RK15-9A	71 Qz, 9 Plg, 20 Kfs	732 876/144 686	MS17-12C	32 Qz, 42 Plg, 26 Hlb	734 127/140 223
RK15-9B	60 Qz, 24 Plg, 15 Kfs, 1 Mica	732 876/144 686	RK15-5	60 Qz, 25 Plg, 15 Mica	732 933/142 432
RK15-10	71 Qz, 19 Plg, 10 Mica	733 398/151 952	RK15-18	16 Qz, 28 Plg, 56 Mica	730 110/142 903
RK15-11A	33 Qz, 32 Pl, 35 Kfs	722 272/152 194	RK15-22	55 Qz, 15 Plg, 30 Mica	729 771/139 042
RK15-17	35 Qz, 43 Plg, 22 Mica	729 661/143 839	RK60	25 Qz, 70 Plg, 5 Cc	726 875/152 275
RK15-20	50 Qz, 41 Plg, 9 Mica	730 265/140 481	RK68	50 Cc, 50 Dol	732 536/149 964
RK15-24B	38 Qz, 52 Plg, 14 Mica	730 008/136 819	RK70A	36 Qz, 38 Plg, 26 Mica	737 323/136 241
RK15-27B	63 Qz, 37 Plg	719 193/152 476	SADU16	42 Qz, 10 Plg 43 Mica, 5 Grt	732 641/134 758
RK15-28	34 Qz, 52 Plg, 14 Mica	719 424/153 347	SADU30	41 Qz, 25 Plg, 34 Mica	731 985/162 618
RK15-30B	29 Qz, 60 Plg, 11 Mica	727 713/156 013	ZAP01	29 Qz, 23 Plg, 37 Mica, 7 Grt, 4 Hbl	near Zapporthütte
RK15-31	76 Qz, 4 Plg, 20 Kfs	727 713/156 835			
RK63B	35 Qz, 32 Plg, 33 Kfs	731 539/148 966	C	Composition in Volume %	Location
RK66	37 Qz, 33 Plg, 30 Kfs	732 554/148 402	RK15-4	7 Qz, 29 Plg, 53 Hbl, 11 Omp	732 078/141 893
SADU39	58 Qz, 25 Plg, 17 Mica	733 687/139 694	RK15-7	15 Qz, 31 Plg, 51 Hbl, 3 Czo	732 467/143 492

251 Table 1: Sample locations in Swiss coordinates and mineral volume percentages of (A) orthogneisses, (B)
252 paragneisses and (C) metabasites. Cc: calcite, Czo: clinozoisite, Dol: dolomite, Grt: garnet, Hbl: hornblende,
253 Kfs: Kalifeldspar, Omp: omphacite, Plg: plagioclase, Qz: quartz.

254

255 The mineral compositions of the paragneisses is more variable. Similar to the orthogneiss samples, the
256 paragneisses consist of quartz, plagioclase and mica, however there is no potassium feldspar in the
257 samples and the mica contents are generally higher (Table 1B). A few samples (RK15-18, SADU16) have a
258 high mica content and therefore represent mica schists. Since they fall into the same category of clastic
259 metasediments, they are summarized as paragneisses which are the predominant rock type of that group.
260 They were also considered for the calculation of the average sample, concerning composition and CPO.
261 White mica is more common within the paragneisses, however, biotite occurs more frequently than in the
262 orthogneisses. One of the paragneiss samples contains hornblende and several of the samples contain
263 garnet. Mica appears more frequently aligned in layers compared to the orthogneisses. Microcracks are
264 mostly parallel to the mica basal plane with some exceptions (Fig. 3D-F). Quartz microstructures are also
265 similar to those of the orthogneisses.
266 The marble sample comprises equal amounts of calcite and dolomite, both of which exhibit an SPO with
267 an alignment in the foliation. The metabasites are strongly retrogressed eclogites consisting of about 50%
268 hornblende and variable amounts of quartz, plagioclase, omphacite and clinozoisite (Table 1C).
269 Hornblende shows an alignment within the foliation plane and is preferentially oriented parallel to the
270 stretching lineation.

271

272 4.2. Crystallographic preferred orientation

273

274 Within the gneiss samples two major CPO patterns occur for quartz. In the first, quartz (0001) yields a
275 maximum between the Z- and Y-directions of the pole figure. This pattern occurs in 55% of the samples
276 containing quartz. In the second pattern, quartz (0001) exhibits peripheral maxima at an angle to the
277 foliation normal, occurring in 45% of the samples (Fig. 4A and APPENDIX). Although both patterns occur

278   throughout the sample set, the former is more common in the paragneisses, while the latter occurs more
279   frequently in the orthogneiss samples. In all samples quartz (0001) and (11-20) show an asymmetry, which
280   represents a sinistral motion indicating a top to the north sense of shear. This is in accordance with
281   literature and shows Zapport phase deformation in the Adula nappe (e.g. Löw, 1987; Meyre et al., 1993;
282   Pleuger et al., 2003). Different orientation patterns of quartz pole figures (10-11) and (01-11) may be
283   attributed to mechanical Dauphiné twinning, or induced by active rhombohedral slip (Wenk et al., 2019).
284   Both biotite and white mica show a strong CPO with a pronounced alignment of their basal planes within
285   the foliation in the gneiss samples (Fig. 4A). It should be noted that in texture analysis (and in texture-
286   based modeling of elastic properties) monoclinic crystals are commonly defined in a first monoclinic
287   setting (Matthies and Wenk, 2009), while a more common second setting is used in this manuscript with
288   (001) as a cleavage plane of mica. Both pagioclase and K-feldspar show a very weak to random CPO with
289   only a few exceptions.
290   The marble sample yields a distinct calcite and dolomite CPO. Calcite exhibits an alignment of (0001) in Z-
291   direction and an alignment of (11-20) in X-direction (Fig. 4C). Both (0001) and (11-20) of dolomite show an
292   angle to the Z- and Y-direction respectively. In the metabasites, hornblende is the only mineral yielding a
293   pronounced CPO (Fig. 4D). It shows a strong alignment of (010) in Z-direction and (001) in X-direction in
294   both samples.
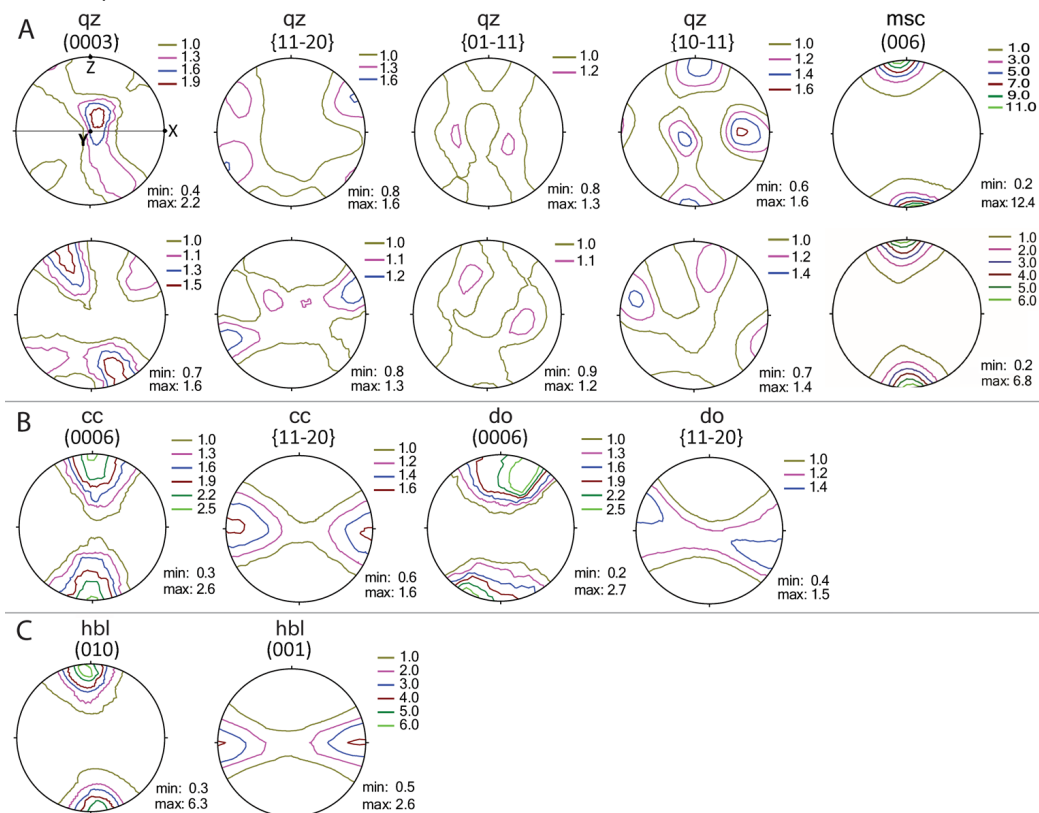
295
296   Figure 4: CPO types in the sample set (A) Common quartz (top: RK15-28; bottom: JK6) and mica (top: RK15-
297   5; bottom: RK15-28) CPO in the orthogneisses and paragneisses; (B) calcite and dolomite CPO in the marble

298   sample (RK68); (C) typical hornblende CPO in the metabasites (RK15-4). All pole figures are lower
299   hemisphere equal area projections. The foliation normal (Z) is vertical, the lineation (X) is horizontal and
300   north is left.
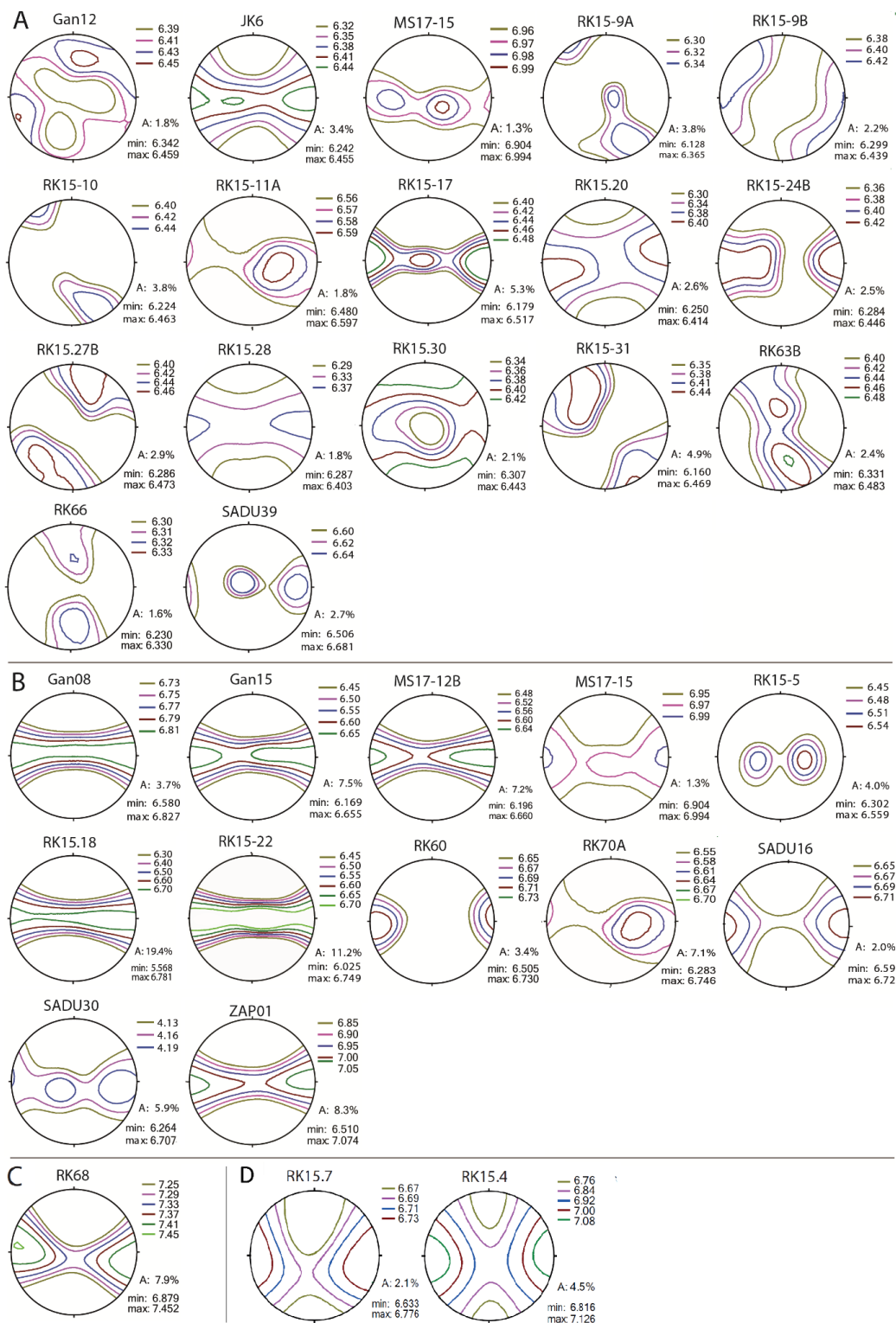
302 Figure 5: Modelled P-wave anisotropies of all natural samples in equal area stereographic projection. (A)
303 Orthogneisses; (B) paragneisses ; (C) marble and (D) metabasites. Contour lines, as well as minima and
304 maxima are in km/sec. The foliation is perpendicular to the projection plane, the lineation is horizontal.
305 XYZ orientation is the same as in Fig. 4.

306

307 4.3. Modeled elastic anisotropies of natural samples

308

309 4.3.1. Orthogneisses

310

311 P-wave anisotropies (AV$_P$) is defined as A = (V$_P$max – V$_P$min)/ V$_P$mean 100%. The orthogneisses show two
312 main patterns, one of which yields highest P-wave velocity (V$_P$) at an angle to the foliation normal, the
313 other exhibits a V$_P$ maximum in lineation direction with a distribution of high V$_P$ values in the foliation
314 plane in some samples (Fig. 5A). The maxima at an angle to the foliation normal are frequently elongated
315 or even show two distinct maxima within an area of higher V$_P$ (GAN12, RK15-9A, RK15-27B). Only few
316 samples deviate from these two patterns showing maxima between the Y direction and the foliation
317 normal (RK63B, RK66) or several maxima within the foliation plane (MS17-15, SADU39). AV$_P$ lies between
318 1.3 and 5.3% with an average of 2.9%. V$_P$/V$_S$ ratios are between 1.51 and 1.67 (Table 2A) with an average
319 of 1.60.

320

A	Vp A (%)	Vs1 A (%)	Vs2 A (%)	VP/Vs	Vp (km/s)	Vs (km/s)	B	Vp A (%)	Vs1 A (%)	Vs2 A (%)	VP/Vs	Vp (km/s)	Vs (km/s)
GAN12	2,5	1,8	1,7	1,57	6,40	4,07	GAN08	3,7	5,0	1,4	1,64	6,73	4,11
JK6	3,4	2,0	3,0	1,63	6,35	3,91	GAN15	7,5	6,7	4,5	1,58	6,43	4,07
MS17-15	1,3	1,0	0,5	1,63	6,95	4,27	MS17-12B	7,2	5,7	3,3	1,57	6,44	4,10
RK15-10	3,8	3,1	2,4	1,53	6,35	4,16	MS17-12C	2,0	1,2	1,2	1,65	6,61	4,01
RK15-11A	1,8	1,0	1,2	1,61	6,55	4,06	RK15-18	20,5	19,4	11,5	1,65	6,18	3,73
RK15-17	5,3	5,0	2,5	1,65	6,35	3,86	RK15-22	11,2	8,0	5,5	1,56	6,42	4,10
RK15-20	2,6	1,5	1,1	1,60	6,33	3,96	RK15-5	4,3	4,0	1,9	1,55	6,42	4,14
RK15-24B	2,5	1,8	2,1	1,64	6,37	3,89	RK60	3,4	2,8	1,5	1,64	6,60	4,03
RK15-27B	2,9	3,6	2,3	1,54	6,39	4,14	RK68	7,9	4,4	2,3	1,82	7,22	3,96
RK15-28	1,8	1,1	1,6	1,64	6,35	3,86	RK70A	7,1	6,1	4,3	1,61	6,53	4,06
RK15-30B	2,1	1,0	0,6	1,67	6,39	3,81	SADU16	2,0	1,5	1,0	1,60	6,65	4,15
RK15-31	4,9	5,4	3,6	1,51	6,33	4,18	SADU30	6,8	5,9	2,7	1,60	6,50	4,07
RK15-9A	3,8	3,2	3,5	1,54	6,26	4,06	ZAP01	8,3	6,6	3,3	1,64	6,81	4,17
RK15-9B	2,2	1,5	1,5	1,57	6,38	4,07							
RK63B	2,4	1,6	1,9	1,63	6,42	3,95	C	Vp A	Vs1 A	Vs2 A	VP/Vs	Vp	Vs
RK66	1,6	1,1	0,8	1,64	6,29	3,83	RK15-4B	4,5	1,7	1,2	1,79	6,94	3,88
SADU39	3,1	2,7	2,0	1,56	6,57	4,21	RK15-7	2,1	0,6	0,7	1,76	6,70	3,81

322 Table 2: P-wave and S-wave anisotropy, VP/VS ratio as well as Voigt average of P-wave and S-wave
323 velocities of (A) orthogneisses, (B) metasediments and (C) metabasites.

324

325 4.3.2. Paragneisses

326

327 The paragneiss samples all show highest V$_P$ value within the foliation plane (Fig. 5B). Most samples also
328 yield a maximum in lineation direction. There are two samples displaying maxima within the foliation plane
329 but not aligned in lineation direction (RK15-5; SADU30). The AV$_P$ of the paragneisses is highly variable
330 ranging from 2.0% to 20.5% (Table 2B). Most samples, however, show a moderate AV$_P$ of 7-8%. V$_P$/V$_S$ ratios
331 lie between 1.55 and 1.65.

332

4.3.3. Marble

333

334

335 The marble sample RK68 exhibits an AV$_P$ of 7.9% with a maximum at a slight angle to the lineation direction
336 and some distribution of high V$_P$ values in the foliation plane (Fig. 5C). Its V$_P$/V$_S$ ratio is 1.82 (Table 2B).

337

4.3.3. Metabasites

338

339

340 The V$_P$ distributions in the metabasites show a pronounced maximum in lineation direction (Fig. 5
341 D). Lowest V$_P$ is found parallel to the foliation normal. AV$_P$ values are 4.5% and 2% with V$_P$/V$_S$ ratios of 1.79
342 and 1.76, respectively (Table 2C).

343

344 4.4. Measured elastic anisotropies of natural samples

345

346 The V$_P$ distribution of the two gneiss samples, which were measured using ultrasound at different confining
347 pressures both show high V$_P$ in the foliation plane. The orthogneiss RK15-17 yields a maximum V$_P$ within
348 the foliation plane at a slight angle to the lineation (Fig. 6A). At maximum pressures of 400 MPa its AV$_P$ is
349 14%. The paragneiss RK15-22 was measured at a maximum pressure of 300 MPa. Maximum V$_P$ is aligned
350 in lineation direction (Fig. 6B). It exhibits an AV$_P$ of 17%. Both samples show increasing V$_P$ values as well as
351 decreasing AV$_P$ coefficients with increasing pressures during the experiment (Table 3). In general, the
352 RK15-17 orthogneiss is elastically more isotropic and shows V$_P$ values comparable to the RK15-22
353 paragneiss at pressures over 100 MPa (Table 3), but at lower pressures P-wave velocities in the orthogneiss
354 decrease drastically, and the elastic anisotropy significantly increases, reaching values much higher than
355 in the paragneiss.

356
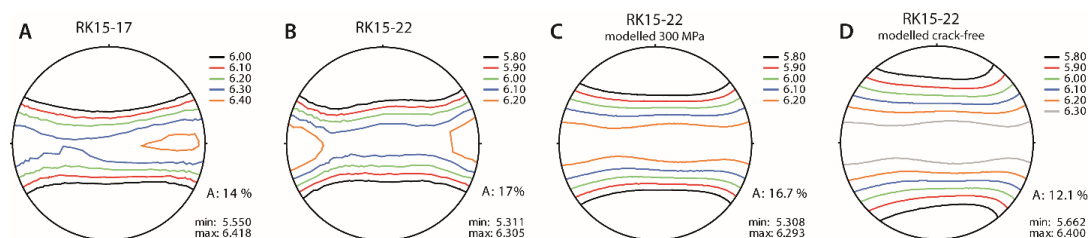
357

358 Figure 6: P-wave anisotropies of an (A) orthogneisses (RK15-17) and a (B) paragneiss (RK15-22) measured
359 using ultrasound. Figures show P-wave distribution at maximum pressures in the experiments. V$_P$
360 distribution of RK15-22 modelled with GMS algorithm at 300MPa (C) and at crack-free pressures (D).
361 Contour lines, as well as minima and maxima are in km/sec. XYZ orientation is the same as in Figs. 4, 5.

362

363 4.5. "Average" rock concept and crack-free "average" rock

364

365 Elastic properties and elastic wave velocities in rocks are normally assessed in laboratory measurements
366 on samples of several cm length. To implement elastic anisotropies in geophysical models these
367 laboratory-derived elastic properties need to be upscaled to a km scale. It is necessary to calculate elastic
368 properties of the rock massif in a long-wavelength approximation (Berryman, 1980), and thus a whole rock

369 massif may be represented as an effective "average" rock. It should feature average CPOs, volume
370 fractions and grain shapes of minerals, as well as average pore and crack patterns.
371

Pressure (MPa)	RK15-17, experiment			RK15-22, experiment			RK15-22, model					
	V_{Pmin} (km/s)	V_{Pmax} (km/s)	AV_P (%)	V_{Pmin} (km/s)	V_{Pmax} (km/s)	AV_P (%)	V_{Pmin} (km/s)	V_{Pmax} (km/s)	AV_P (%)	Type I crack density	Type II crack density	Total crack porosity
5				3.656	5.242	35	3.662	5.244	36	0.246	0.057	0.0163
10	2.637	4.459	51	3.904	5.349	31	3.904	5.350	31	0.205	0.056	0.0145
20	3.207	4.812	40	4.194	5.520	27	4.196	5.524	27	0.162	0.048	0.0118
50	4.106	5.316	26	4.584	5.786	23	4.583	5.791	23	0.112	0.031	0.0079
100	4.787	5.824	20	4.902	6.019	20	4.915	6.037	20	0.074	0.014	0.0046
200	5.307	6.203	16	5.202	6.269	19	5.213	6.263	18	0.043	0	0.0018
300	5.501	6.339	14	5.311	6.305	17	5.307	6.293	17	0.033	0	0.0014
400	5.550	6.418	14									
Crack free							5.662	6.400	12	0	0	0

372
373 Table 3: Results of ultrasonic measurements of (A) orthogneiss RK15-17 and (B) paragneiss RK15-22
374 showing V_P and AV_P at increasing pressures. (C) V_P and AV_P of RK15-22 modelled with GMS algorithm.
375

376 As a first approximation to the crustal properties, only major minerals were considered for the "average"
377 rock: plagioclase, muscovite and quartz. Minor or uncommon mineral phases were omitted. From the
378 selection of 30 natural crustal rocks, we identified characteristic CPO types and average CPO strengths for
379 all common mineral phases. In general, feldspar shows weak to random CPO, even in strongly deformed
380 samples. Furthermore, only minor differences have been observed between plagioclase and potassium
381 feldspar. Therefore, the ODF of a representative plagioclase with weak texture was chosen for the
382 "average" rock, namely, the albite ODF in RK15-28 sample. Since white mica is most common in both
383 orthogneisses and paragneisses, muscovite was chosen as representative mica for the average rock. In all
384 samples mica shows a pronounced alignment of its basal plane in the foliation. The mica ODF of two
385 samples (RK15-5; RK15-28) was combined in 1:1 ratio to yield an average preferred orientation for the
386 "average" sample. Likewise, the representative quartz ODF for the average sample was chosen as a
387 combination of CPOs from two different samples (JK6; RK15-28) in 5:6 ratio. These two samples show the
388 typical quartz CPO patterns mentioned in section 4.4 and shown in Fig. 4A.
389 Based on analysis of all samples, average mineral volume percentages in gneisses (43% quartz, 40%
390 plagioclase, 17% mica) were considered for the "average" rock. Corresponding density value is 2670.7
391 kg/m³. For the GMS method, grain shapes of minerals should be approximated by ellipsoids. Thin section
392 analysis of samples revealed more or less equiaxed grain shapes of quartz and feldspar and elongated mica
393 platelets with average aspect ratio of ≈0.2 (APPENDIX – Fig 1). Numerical models revealed that aspect
394 ratios of grains of mica and quartz within 0.1-1 range have only minor influence on bulk elastic properties
395 (Nishizawa and Yoshino, 2001; Vasin et al., 2013; Huang et al., 2021). Consequently, for the "average" rock,
396 we considered spherical grains of quartz and feldspar, and oblate spheroidal grains with axes ratio 1:1:0.2
397 for mica. As the shape of mica grains is related to cleavage, the corresponding SPO may be derived from
398 CPO by considering additional rotation of the crystallite coordinate system (Vasin et al., 2013).
399 The preferred orientations, mineral volume fractions and grain shapes were combined in a model of the
400 elastic properties for the "average" rock using the GMS approach. The V_P distribution in a crack-free
401 "average" rock is shown in Figure 7. There is a distribution of high V_P values within the foliation plane, and
402 the maximum V_P direction is located between the lineation (X-direction) and the Y-direction. The AV_P of
403 the "average" crack-free gneiss is 4%.
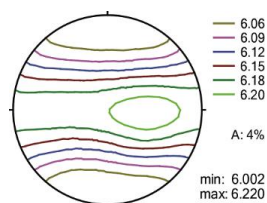
404
405 Figure 7: Modelled P-wave anisotropies of an average gneiss at 740 MPa. Contour lines, as well as minima
406 and maxima are in km/sec. XYZ orientation is the same as in Fig. 4.
407

408 4.6. "Average" rock with microcrack systems
409

410 As directly evident from thin sections analysis (Figure 3), low aspect ratio microcracks are present in the
411 samples. At low overburden depths, these microcracks are open. As seen from Table 3, at low pressures
412 measured elastic wave velocities are decreased and elastic anisotropy is increased compared to the high
413 pressure, where majority of microcracks are closed. To account for the changes of elastic anisotropy of the
414 "average" rock due to pressure/depth changes, it is necessary to include these microcracks and their
415 closure with increasing pressure into the model.
416

Pressure (MPa)	Depth (km)	Density (kg/m^3)	Type I crack density	Type II crack density	Total crack porosity	V_{Pmin} (km/s)	V_{Pmax} (km/s)	AV_P (%)
5	0.2	2627.19	0.246	0.057	0.0163	4.203	4.728	12
10	0.4	2631.99	0.205	0.056	0.0145	4.442	4.891	10
20	0.8	2639.21	0.162	0.048	0.0118	4.721	5.121	8
50	1.9	2649.62	0.112	0.031	0.0079	5.077	5.454	7
100	3.8	2658.43	0.074	0.014	0.0046	5.372	5.748	7
200	7.6	2665.91	0.043	0	0.0018	5.630	6.012	7
300	11.5	2666.98	0.033	0	0.0014	5.709	6.057	6
≈740	28.2	2670.72	0	0	0	6.002	6.220	4

417
418 Table 4: V_P, AV_P, and crack densities of "average" rock model at increasing pressures including
419 corresponding depth. 740 MPa is an estimation of the pressure where the cracks are closed (see text).
420 Cracks type I have the same ODF as mica.
421

422 As a first approximation, we considered that the "average" rock should have the same crack distribution
423 as one of the characteristic gneiss samples, i.e., sample RK15-22. From thin sections analysis (Figure 3D-
424 F), two possible microcrack systems were identified. There is one set of microcracks mostly oriented along
425 the muscovite platelets, and we denote these as type I cracks. Type I cracks were assumed to have the
426 same SPO as muscovite grains; and their aspect ratio was estimated to be ≈0.01 (Appendix – Fig 2). As
427 these cracks are roughly parallel to mica platelets, within the GMS algorithm type I cracks were
428 approximated by oblate ellipsoids with an axial ratio of 1:1:0.01. Another set of cracks – denoted as type
429 II cracks - intersects quartz grains, they are mostly oriented parallel to the Z axis. They display a broader
430 range of aspect ratios with an average of ≈0.025 (Appendix – Fig 1). Since these cracks are mostly within
431 equiaxed quartz grains, they were approximated by oblate ellipsoids with an axial ratio of 1:1:0.025. To
432 determine the changes of crack densities of type I and II with pressure, a following procedure was applied.

433   Elastic properties of a crack-free RK15-22 gneiss were modelled with GMS algorithm using measured ODFs,
434   mineral volume fractions (55% quartz, 15% albite and 30% muscovite), and assuming spherical grain
435   shapes for quartz and albite, and 1:1:0.2 ellipsoidal grains for muscovite. Using mineral density values from
436   the same references as mineral single crystal elastic properties, a density of 2702.3 kg/m^3 was computed
437   for a crack-free RK15-22. Using model elastic properties and this density value, the V_P distribution in a
438   crack-free RK15-22 was calculated (Fig. 6C).

439   Density measurements of RK15-22 at atmospheric pressure yield a value of 2658 kg/m^3. Thus, crack
440   porosity in RK15-22 is restricted to a maximum of about ~1.7%. Consequently, type I and type II cracks
441   were added into the model crack-free RK15-22 gneiss to reproduce measured V_P distributions at different
442   pressures, similar to the procedure of porous polycrystalline graphite (Matthies, 2012). The only varying
443   parameters are the type I and type II crack porosities, with the total crack porosity within the
444   aforementioned limit. Using this procedure, an adequate description of experimental V_P distributions with
445   the GMS approach was achieved at all pressures above 2 MPa. The wave velocities and AV_P values of RK15-
446   22 models are given in Table 3.

447

Pressure (MPa)	C_{11} (GPa)	C_{12} (GPa)	C_{13} (GPa)	C_{14} (GPa)	C_{15} (GPa)	C_{16} (GPa)	C_{22} (GPa)	C_{23} (GPa)	C_{24} (GPa)	C_{25} (GPa)	C_{26} (GPa)	C_{33} (GPa)	C_{34} (GPa)	C_{35} (GPa)	C_{36} (GPa)
5	58.0	9.1	7.8	0.1	-0.1	-0.2	58.1	7.9	0.2	-0.1	-0.3	46.4	0.1	-0.1	0.0
10	62.2	10.2	9.0	0.1	-0.1	-0.2	62.4	9.0	0.2	-0.1	-0.3	51.9	0.1	-0.1	0.0
20	68.4	11.8	10.6	0.1	-0.1	-0.2	68.6	10.6	0.2	-0.1	-0.3	58.8	0.1	-0.1	0.0
50	77.9	14.6	13.3	0.1	0.0	-0.2	78.2	13.3	0.2	-0.1	-0.3	68.3	0.1	-0.1	0.0
100	86.8	17.5	16.1	0.1	0.0	-0.1	87.1	16.2	0.2	-0.1	-0.4	76.7	0.1	-0.1	0.0
200	95.2	20.7	19.1	0.1	0.0	-0.1	95.6	19.1	0.2	-0.1	-0.4	84.5	0.0	-0.1	0.0
300	96.7	21.3	19.8	0.1	0.0	-0.1	97.1	19.9	0.2	-0.1	-0.4	86.9	0.0	-0.1	0.0
≈740	102.2	23.7	22.9	0.0	0.1	-0.1	102.6	23.0	0.1	-0.1	-0.4	96.2	0.0	-0.1	0.0

continuation

Pressure (MPa)	C_{44} (GPa)	C_{45} (GPa)	C_{46} (GPa)	C_{55} (GPa)	C_{56} (GPa)	C_{66} (GPa)
5	21.5	-0.1	-0.1	21.4	0.1	24.6
10	23.4	-0.1	-0.1	23.2	0.1	26.2
20	25.8	-0.1	-0.1	25.6	0.1	28.5
50	29.1	-0.1	-0.1	28.9	0.1	31.9
100	32.0	-0.1	-0.1	31.7	0.1	35.0
200	34.5	-0.1	-0.1	34.2	0.1	37.7
300	35.1	-0.1	-0.1	34.8	0.1	38.1
≈740	37.3	-0.1	-0.1	36.9	0.1	39.7

448
449   Table 5: Bulk elastic tensor components of the "average" rock model, rounded to first decimal digit.

450

451   At maximum pressure of 300 MPa the experimental V_P values are 0.3-0.7 km/s lower than corresponding
452   velocities in the crack-free RK15-22 with biggest differences for minimum velocities. This implies a small
453   amount of open microcracks. Modeling suggests that type II cracks with 0.025 aspect ratio are not
454   necessary to describe bulk elastic properties of RK15-22 sample at pressures of 200 MPa and higher. Thus,
455   we assume that type II crack porosity is close to zero at 300 MPa. Since type I cracks orientation distribution
456   is not random, and the material is elastically anisotropic with AV_P =17%, only a rough estimation of type I
457   cracks closure pressure can be made. We averaged the stiffness tensor of crack-free RK15-22 over all
458   directions and applied the relation derived by Walsh (1965) for an isotropic rock to obtain a closure
459   pressure of ≈740 MPa for type I cracks at an aspect ratio of 0.01. Thus, we assume that the RK15-22 gneiss
460   may be considered crack free at a pressure of 740 MPa.

461 It is recognized that at low crack porosities effective elastic properties of the material depend on the crack
462 density, while crack porosity is irrelevant (Vernik, 2016; Kachanov and Mishakin, 2019). Crack porosity and
463 crack density may be related for certain types and distributions of cracks. E.g., in the case where all cracks
464 have the same aspect ratio, as type I or type II pores separately, there is a simple equation (Lokajicek et
465 al., 2021) connecting crack porosity and crack density. Thus, in Table 4, crack densities are given for type I
466 and type II cracks separately, as well as the total crack porosity. We assume that the same system of cracks
467 exists in an "average" sample such as RK15-22, with the same orientation distribution and the same crack
468 density values at corresponding confining pressure. The GMS algorithm was used to add this crack system
469 to the crack-free "average" rock, and the density of the crack-free "average" rock was used to estimate
470 the overburden from the pressure values. From that, the dependencies of all stiffness tensor components
471 of the "average" rock on depth were obtained, as well as the elastic wave velocities and the AV_P
472 coefficients (Tables 4 and 5).

474 5. Discussion

476 There are various factors influencing the elastic anisotropy of rocks. While the deformation induced CPO
477 is the main cause, there are other aspects like shape preferred orientation (SPO) of grains, or layering
478 contributing to elastic anisotropy. Another important factor influencing elastic anisotropy, especially at
479 lower depth is the occurrence of microcracks. In the following, we discuss the elastic anisotropies -
480 calculated and measured - of the natural samples from this study. We will elaborate the applicability of
481 the model "average" rock to larger scale crustal rock units and discuss the controlling factors of the elastic
482 anisotropy of crustal rocks.

484 5.1. Elastic anisotropy of natural samples

486 5.1.1. Orthogneisses

488 The AV_P calculated from the CPO data of orthogneisses is largely influenced by CPOs of quartz and mica.
489 Since feldspar generally shows weak or no CPO, its presence in the samples mainly contributes to a
490 decrease in AV_P. Mica adds to increased V_P values within the foliation plane as well as the maxima in
491 lineation direction in some samples. Highest V_P is found within the basal plane of mica single crystals,
492 which defines the V_P pattern caused by observed alignment of mica basal planes within the foliation. The
493 maxima in lineation direction are caused by a slight tilting of mica basal planes around the lineation. This
494 leads to broadening of high V_P region within the YZ-plane and results in the highest V_P in lineation direction.
495 Highest V_P values of quartz single crystals are observed close to normals to their rhombohedral planes.
496 Patterns showing elongated V_P maxima close to the periphery at an angle to the foliation and the patterns
497 with several maxima for V_P are due to the influence of quartz CPO. The frequently observed asymmetry in
498 these patterns with respect to the reference frame of foliation and lineation reflects non-coaxial
499 deformation of the rocks. All units in the central Adula Nappe show a top-to-the-north sense of shear (e.g.
500 Nagel, 2008), thereby producing asymmetric quartz CPO, which in turn leads to the asymmetric V_P
501 distributions in the mica-poor orthogneisses. Both AV_P as well as V_P patterns are similar to those in
502 previous studies, which either show high V_P in the foliation with a maximum in lineation direction (Ivankina

503   et al. 2005; Ullemeyer et al., 2006; Kern et al. 2008; Zel et al., 2015; Ivankina et al., 2017; Schmidtke et al.,
504   submitted to same issue), at an angle to the lineation (Vasin et al., 2017), or elongated asymmetric maxima
505   between the foliation normal and the foliation plane (Ullemeyer st al., 2006; Llana-Fúnez et al., 2009).
506   The orthogneiss sample RK15-17 measured in the lab shows high V_P distributed within the foliation plane
507   with a maximum at a slight angle to lineation direction. While both the measured and the calculated
508   velocity patterns for this sample show high V_P distributed in the foliation plane, the AV_P pattern calculated
509   from CPO yields its maximum aligned in lineation direction with an additional maximum in Y-direction. The
510   AV_P coefficient calculated from measured P-wave velocities at a pressure of 400 MPa is higher than the
511   calculated one by a factor 2.6, which is mostly due to still open microcracks, not considered within the
512   Voigt averaging scheme. Due to a preferred orientation of microcracks parallel to the mica basal plane
513   (Fig. 3A-C) and an alignment of mica in the foliation V_P is slower normal to the foliation and AV_P is higher
514   in the samples measured in the lab, even at the highest pressures.
515   V_P/V_S ratios in the orthogneiss samples are influenced by the volume percentage of the constituent mineral
516   phases. Due to the low Poisson ratio of quartz and its generally large volume percentage in the
517   orthogneisses their V_P/V_S ratios of 1.51-1.67 are low.
518
519   5.1.2. Paragneisses
520
521   Like in the orthogneisses, the V_P pattern of the paragneisses and micaschists is influenced by mica and
522   quartz CPO with a larger mica contribution due to its generally higher volume content in paragneisses
523   compared to the orthogneisses (Table 1B). Likewise, mica CPO leads to high V_P values within the foliation
524   plane and frequently to a V_P maximum in lineation direction. This V_P pattern is similar to that of
525   paragneisses in previous studies (e.g. Weiss et al., 1999; Erdman et al., 2013; Keppler et al., 2015;
526   Ullemeyer et al., 2018). V_P patterns showing maxima within the foliation plane, but not aligned with the
527   lineation, are likely caused by a discrepancy between CPO formation of quartz and CPO formation of mica.
528   The samples are oriented according to their visible mineral stretching lineation, which was formed by
529   quartz in most samples. The alignment of high velocities is, however, caused mostly by mica CPO and
530   undulating mica grains around the stretching lineation. The CPO of quartz and mica was not necessarily
531   formed at the same time and could represent different deformation stages.
532   The sample measured in the lab, RK15-22, similar to the case of the orthogneiss sample, shows a higher
533   influence of mica on AV_P due to its alignment in the foliation and similarly oriented microcracks. While in
534   the calculated V_P distribution, high velocities are distributed within the foliation plane, the measured
535   velocities show a distinct maximum in lineation direction. The measured version also shows a higher AV_P
536   than the one calculated from the CPO. The difference, however, is not as large as for the orthogneiss
537   sample. In case of the paragneiss sample the measured AV_P is higher than the calculated one by a factor
538   of 1.5. Similar to the orthogneisses, this value is well in the range of other literature comparing
539   experimental and modeled anisotropy data. While experimental anisotropies are always higher than the
540   ones modeled using CPO, the factor is variable for gneiss samples ranging from 1.3 (e.g. Vasin et al., 2017)
541   to 6.6 (e.g. Ullemeyer et al., 2006). Considering experimental and modeled elastic anisotropy data of 18
542   gneiss samples from different studies, experimental anisotropy is 3 times higher than the modeled ones
543   on average (Ivankina et al., 2005; 2017; Punturo et al., 2005; Ullemeyer et al., 2006; 2018; Kern et al., 2008;
544   Kern, 2009; Llana-Fúnez et al., 2009; Lokajicek et al., 2014; Zel et al., 2015; Vasin et al., 2017). V_P/V_S ratios

545   of the paragneisses are determined by the volume percentage of quartz and yield values of 1.55-1.64.
546   Higher volume percentages of quartz lead to lower V_P/V_S ratios.
547   Comparing the V_P velocities calculated from the Voigt model (Figure 5B) and the GMS crack free model
548   (Table 3) of the RK15-22 sample, it is evident that the Voigt model velocities are ≈300-400 m/s higher. Yet,
549   symmetries of velocity distributions and AV_P coefficients computed using these two models are quite close,
550   suggesting that the Voigt modeling is reliable to assess the degree of elastic anisotropy of gneisses.
551   Tables 3 and 4 demonstrate a correlation of measured ultrasonic wave velocities and their anisotropy in
552   RK15-22 gneiss as well as the GMS model utilizing the two types of cracks discussed earlier at pressures of
553   5-300 MPa. At 2 MPa, and also at atmospheric pressure, the proposed model was not able to correctly
554   reproduce experimental V_P patterns. At low confining pressure it is observed that both self-consistent and
555   non-interactive theories may be inadequate to describe the elastic velocity behavior, which is mainly due
556   to a lack of knowledge of crack geometries (Hadley, 1976). It is likely that another system of thinner
557   microcracks is required to match the GMS model and experimental ultrasonic wave velocities in RK15-22
558   at low pressure values.
559   As expected, the GMS models of RK15-22 at higher pressure require lower crack densities/porosities to
560   describe the experimental ultrasonic data. Modeling suggests that thinner type I cracks are closed at a
561   faster rate with increasing pressure compared to thicker type II cracks. Yet, due to an initially lower crack
562   density of type II cracks, the modeling suggests that their influence on the bulk elastic properties of model
563   RK15-22 gneiss becomes negligible at and above a pressure of 200 MPa. In contrast, type I cracks are
564   necessary to match the experimental and model P-wave velocities at a pressure of 300 MPa and we could
565   only roughly estimate that these cracks will be closed at a pressure of ≈740 MPa.
566   Naturally, the proposed model is quite simplistic, neglecting, e.g., the distribution of microcracks with
567   respect to shape, deviations of the assumed SPOs of the cracks from those actually present in the gneiss,
568   possible dependence of microcrack SPO on shape of cracks, and changes of all these parameters with
569   pressure. Our results suggest that even small open crack densities at relatively high confining pressures
570   have a notable influence on the elastic anisotropy of the paragneiss. Therefore, a precise quantification of
571   the microcrack characteristics is necessary to simulate realistic models of pressure dependencies on the
572   bulk elastic properties of rocks.
573
574   5.1.3. Marble
575
576   In the marble sample, the maximum V_P is at a slight angle to the lineation caused by the influence of both
577   the dolomite and the calcite CPO. The AV_P of marble in the literature is highly variable depending on the
578   grade of deformation (Burlini and Kunze, 1999; Zappone et al., 2000; Punturo et al., 2005; Schmidkte et al.
579   in prep). Since the marble lenses in the Adula Nappe only make up a few meters in thickness they do not
580   contribute to the overall anisotropy of the unit in any significant amount. The sample yields a high V_P/V_S
581   ratio of 1.82, which is influenced by both calcite and dolomite. These high V_P/V_S ratios are typical for
582   marble (e.g. Keppler et al., 2015).
583
584   5.1.4. Metabasites
585

586   The AV$_P$ of the metabasites is determined by hornblende, which has the highest volume percentage and is
587   the only mineral showing a strong CPO. Highest VP is found within the lineation and caused by the
588   alignment of (001), which is close to the highest VP in hornblende single crystals. Due to the stronger
589   hornblende CPO of RK15-4, the AV$_P$ is higher in this sample. Studies on elastic anisotropies of metabasites
590   mainly focus on eclogites and blueschists (e.g. Abalos et al., 2010; Bezacier et al., 2010; Keppler et al.,
591   2017; Zernati et al., 2019). Many of the metabasic units exhumed during continental collision, however,
592   are strongly retrogressed with large amounts of amphibole and/or chlorite. Recent studies show that these
593   retrogressed rocks frequently show higher elastic anisotropy than pristine basalts, gabbros or also
594   eclogites due to higher elastic anisotropy of amphiboles compared to pyroxenes, as well as a pronounced
595   deformation during exhumation (e.g. Park and Jung, 2020; Schmidtke et al. submitted to same issue). V$_P$/V$_S$
596   ratios of 1.79 and 1.76 for RK15-4 and RK15-7, respectively, are typical for metabasites (e.g. Worthington
597   et al., 2013; Schmidtke et al submitted to same issue).

598

599   5.2. Elastic anisotropy of the modeled "average" rock

600

601   Realistic upscaling of the rock elastic properties measured within limited scale or on laboratory samples
602   to the seismic scale is of a long-standing interest, e.g., in hydrocarbon reservoirs (Sayers, 1998; Bayuk et
603   al., 2008; Avseth et al., 2010). Here, we consider a rather homogeneous crystalline rock with low crack
604   porosity, and we try to build an effective large-scale model using features of the studied rock massif:
605   average mineral volume fractions, preferred orientations, grain shapes and microcracks systems.
606   As expected, the "average" rock shows a distribution of high V$_P$ values normal to the Z-axis due to the
607   preferred orientation of mica, with a maximum V$_P$ value at an angle to the X-axis due to the influence of
608   the preferred orientation of quartz (Fig. 7). This is a common pattern in the natural sample set (Fig. 5A
609   and B). The model suggests decreasing AV$_P$ and increasing V$_P$ values with increasing depth due to the
610   closure of microcracks. A crack free "average" rock has V$_P$ values slightly over 6 km/s and a rather low AV$_P$
611   of 4%, which is in between AV$_P$ values characteristic for paragneisses and orthogneisses. At lower confining
612   pressure down to 5 MPa (corresponding to a depth of ≈ 200 m), the model suggests a decrease of V$_P$ values
613   to ~4.5 km/s, and an increase of AV$_P$ to 12% (Table 4) due to open microcracks.
614   Some orthogneisses in the natural sample set show maxima at an angle to the foliation normal, which is
615   different from the average sample (Fig. 5A). However, these samples generally show a low AV$_P$ and do not
616   strongly contribute to the overall anisotropy.
617   What are the limitations of the proposed model? As discussed in 5.1.2, one of the main improvements
618   may be made by better quantification of microcrack systems. Crack closure with increasing pressure in
619   anisotropic gneisses should be studied in more detail to reliably expand the crack closure in RK15-22
620   paragneiss to the rock massif in general. Further model improvement may be achieved by more detailed
621   constraints on the mineral volume fractions and crystallographic textures within the rock massif via more
622   extensive sampling.
623   The calculated "average" rock model is related to the XYZ coordinate frame, defined by rock foliation and
624   lineation. To improve the model, it is necessary to account for possible foliation or lineation direction
625   changes through the rock massif by relating all crystal and shape preferred orientations to the same global
626   reference frame, e.g., geographical coordinates.

627   It is evident that the calculated model of the "average" rock does not consider large scale layering. It may
628   be introduced into the model by creating "average" rock layers consisting of the characteristic minerals
629   with their preferred orientations and microstructures and using a Backus averaging to combine thin
630   (relative to the lateral size) rock layers into a seismic scale effective medium (Sayers, 1998). Furthermore,
631   large scale faults are an important factor when considering elastic anisotropy and have to be considered
632   in any model of the Alps. Finally, only pressures and the density of the crack-free "average" rock were used
633   to estimate the depth values. Compositional variations would change the depth estimates.
634   Despite all these simplifications of the current model, in principle, the proposed "average" rock may be
635   constructed to represent effective elastic properties on any necessary scale if there is sufficient
636   information on modal composition, textures and microstructures available from the selected samples. It
637   would be interesting to make a direct comparison of the "average" rock with seismic data on the
638   uppermost layer of the crust.
639
640   5.3. Elastic anisotropy in the Alps
641
642   The well-studied geology of the Alps provides comprehensive foliation and lineation maps (e.g., Steck
643   1990). Surface data can be correlated with seismic imaging making it possible to construct models for
644   different tectonic structures at depth (e.g. Yosefnejad et al., 2017). For the present study, the Adula Nappe
645   was chosen as a representative unit for deformed upper crust in the Alps. The central part of the Adula
646   Nappe, where the samples for this study have been collected exhibits a shallowly NE dipping foliation and
647   a NS trending lineation mainly formed during peak pressure and early stages of exhumation. Parts of the
648   nappe further to the north as well as the south, however, have been overprinted by younger deformation
649   (e.g. Löw, 1987; Nagel, 2008; Kossak et al. 2017).
650   The afore mentioned discrepancy between quartz lineation and mica CPO in several of the samples has
651   not well been studied with respect to the seismic anisotropy. It could be a common issue for most upper
652   crustal units in the Alps, exhibiting a complicated deformation history. Hence, maxima for elastic
653   anisotropies in lineation direction in mica rich rocks cannot simply be correlated to measurements in the
654   field.
655   Microcrack distribution and orientation have not been investigated systematically throughout the rock
656   units of the Alps and they might exhibit strong local variations corresponding to the large-scale fracture
657   and fault pattern (e.g. Vilhelm et al., 2010). This has also a great effect on the travel times of P- and S-
658   waves, i.e. V_P and V_S are significantly decreased (e.g. Yan et al., 2005; Kelly et al., 2017) and therefore
659   needs to be considered for any large-scale section or model of the Alps (e.g. TRANSALP: Lüschen et al.,
660   2004; Millahn et al., 2005; AlpArray: Hetényi et al., 2018; Molinari et al., 2020).
661   While deformed granitoids (e.g. orthogneisses) and deformed clastic metasediments (e.g. paragneisses)
662   are the dominant lithologies, the rock spectrum found in the Alps and other collisional orogens ranges
663   from sedimentary rocks as well as metasediments like marbles, micaschists and quartzites, over
664   metabasites like eclogites, blueschists, amphibolites and greenschists to ultrabasic rocks like peridotites
665   and serpentinites. Furtheremore, volcanic and plutonic intrusions are a common occurrence in collisional
666   orogens.
667   There are several nappes within the Alps dominated by (meta-)basic (e.g. the Zermatt–Saas zone:
668   Angiboust et al., 2009) and ultrabasic rocks (e.g. the Ivrea Complex: Hartmann and Wedepohl, 1993), which

669   have to be considered in some seismic profiles across the Alps. While we present data on some common
670   minor lithologies, like amphibolite, marble and micaschist, we also refer the reader to data on
671   metasediments (e.g. Punturo et al., 2005), metabasites (e.g. Abalos et al., 2010; Bezacier et al., 2010;
672   Zertani et al., 2020; Schmidtke et al., submitted to same issue) and ultrabasic rocks (Mainprice et al. 2000;
673   Ullemeyer et al., 2010). Within the NFP20 EAST profile considered in the present study, amphibolites and
674   marbles mostly occur as small lenses of under 1 km of thickness and are likely not detectable with seismic
675   imaging at depth. The elastic anisotropy of gneiss is therefore decisive for the investigated part of the
676   section. Gneiss samples in this as well as previous studies generally show an alignment of high V_P within
677   the foliation plane. That is why the foliation of gneisses and mica schists formed during continental
678   collision and exhumation is likely a main factor controlling the elastic anisotropies of the continental crust
679   in collisional orogens. The data presented in this study yield a first approximation for average upper crustal
680   seismic properties with increasing depth as well as the specific seismic property spectrum of this deformed
681   upper crustal section of the Alps.
682
683
684   6. Summary and Conclusion
685
686   1. The investigation of a large set of rocks collected in the Adula Nappe, which is considered to be
687   representative of deformed upper crustal rocks in the Alps, indicates a large variety of elastic anisotropies.
688
689   2. The Adula Nappe is mostly made up of orthogneisses with modelled AVP between 1.3 and 5.3% and
690   Vp/Vs ratios between 1.51 and 1.67, as well as paragneisses with modelled AVP between 2.0% to 20.5%
691   and Vp/Vs ratios between 1.55 and 1.65.
692
693   3. Small lenses of less than 100 m thick metabasites show an AVP of 2-4.5% and VP/VS ratios of 1.76-1.79.
694   Marble lenses of even smaller dimensions yield an AVP of 3.4% and VP/VS ratio of 1.83. Yet, these lenses
695   are statistically insignificant for the considered section of para- and orthogneisses.
696
697   4. Orthogneiss and paragneiss measured in the lab using ultrasound both show higher AVP as well as lower
698   VP compared to the ones modelled using CPO, which is caused by open microcracks in the rocks at shallow
699   depth.
700
701   5. Average elastic anisotropies were calculated for a typical gneiss using common CPO types of constituent
702   mineral phases, mineral content, grain shapes and crack systems within the sample set. Calculated elastic
703   constants are considered to be representative for the range of depths from a few hundred meters up to
704   ≈28 km. The modelled "average" gneiss yields an AV_P of 4% at a depth of ≈28 km, where the vast majority
705   of microcracks is closed. Due to the opening of microcracks, the elastic anisotropy of the model gneiss
706   increases towards shallower depth and reaches AV_P = 12% at ≈0.2 km.
707
708

709   Acknowledgement
710

711 This study was funded by the German research foundation (DFG-grant No. KE 2268/2-1, STI298/9-1) as
712 part of the DFG priority programme "Mountain Building Processes in 4 Dimensions". Fruitful discussions
713 within the priority programme are gratefully acknowledged. Furthermore, this study was partially
714 supported by the Czech Science Foundation research grants 18-08826S, 21-26542S and by the Czech
715 Academy of Sciences project RVO 67985831. Authors appreciate the access to the SKAT diffractometer at
716 FLNP JINR. The project was partially supported by the JINR theme No. 04-4-1121-2015/2020.
717

718   APPENDIX
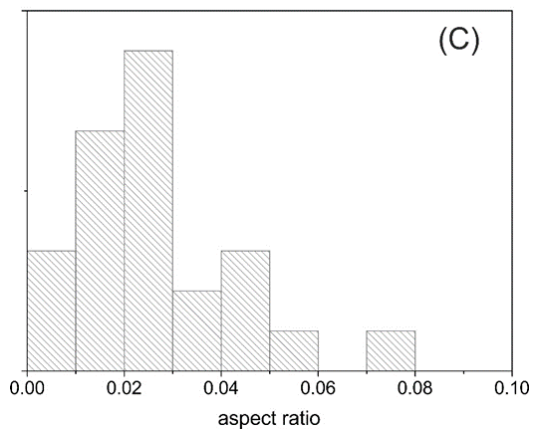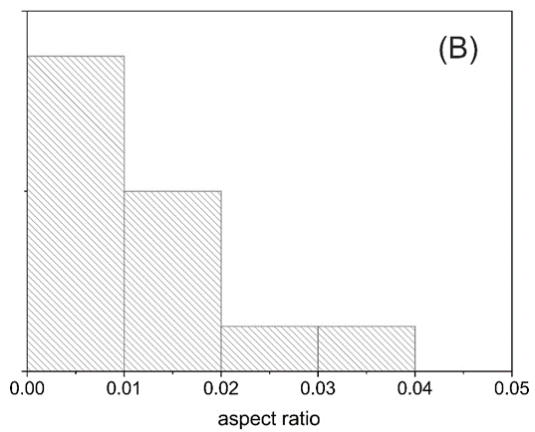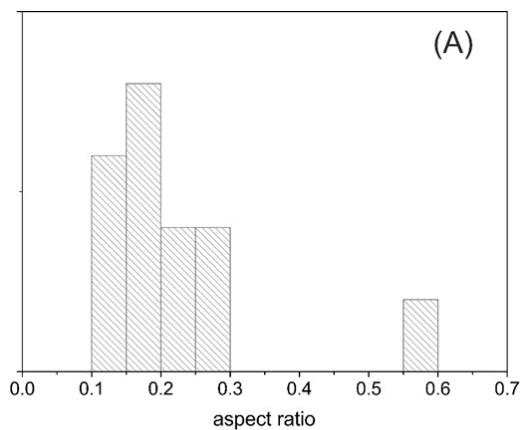
719

720 APPENDIX - Figure 1: Distributions of aspect ratios of mica grains (A), type I (B) and type II (C) cracks based
721 on analysis of several RK15-22 thin sections.
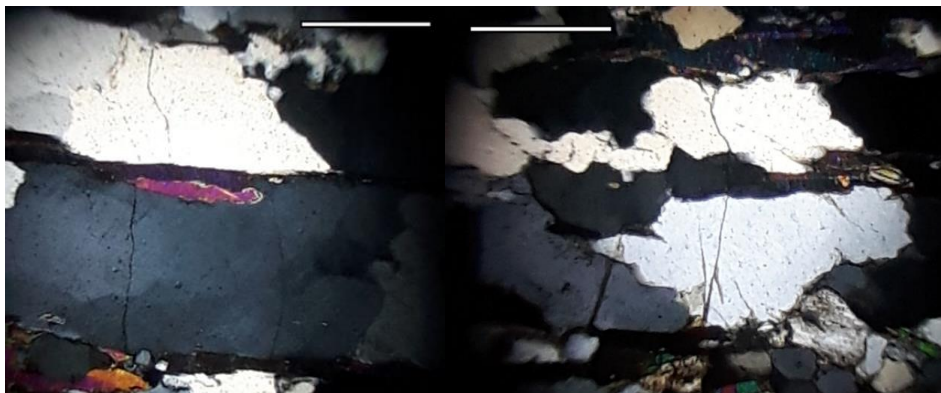
722

723 APPENDIX – Figure 2: Grains of quartz crossed by type II cracks, XZ plane. White scale bar is 0.4 mm.

724 REFERENCES:

726 Ábalos, B., D. M. Fountain, J. I. Gil Ibarguchi, and P. Puelles: Eclogite as a seismic marker in subduction
727 channels: Seismic velocities,anisotropy, and petrofabric of Cabo Ortegal eclogite tectonite (Spain), Geol.
728 Soc. Am. Bull., 123, 439–456, 2010.

730 Abrecht, J.: Geologic units of the Aar massif and their pre-Alpine rock associations: a critical review,
731 Schweiz. Mineral. Petrogr. Mitt., 74, 5-27, 1994.

733 Aleksandrov, K.S., Alchikov, U.V., Belikov, B.P., Zaslavski, B.I., and Krupny, A.I.: Elastic wave velocities in
734 minerals at atmospheric pressure and increasing precision of elastic constants by means of EVM, Izvestija
735 Academy of Science USSR, Geol. Ser. 10, 15–24, 1974.

737 Aleksandrov, K.S., and Ryzhova, T.V.: The elastic properties of rock forming minerals, Izvestija Academy of
738 Science USSR, Geophys. Ser. 12, 1799–1804, 1961.

740 Almqvist, B. S.G., Hirt, A. M., Herwegh, M., Ebert, A., Walter, J. M.; Leiss, B., Burlini, L.: Seismic anisotropy
741 in the Morcles nappe shear zone: Implications for seismic imaging of crustal scale shear zones,
742 Tectonophysics, 603, pp. 162-178, 2013.

744 Almqvist, B. S.G., and Mainprice, D.: Seismic properties and anisotropy of the continental crust: Predictions
745 based on mineral texture and rock microstructure, Reviews of Geophysics, 55, pp. 367-433, 2017.

747 Angiboust S., Agard P., Jolivet L. and Beyssac O.: The Zermatt-Saas ophiolite: the largest (60-km wide) and
748 deepest (c. 70–80 km) continuous slice of oceanic lithosphere detached from a subduction zone? Terra
749 Nova 21, 171–180, 2009.

751 Avseth, P., Mukerji, T., Mavko, G., and Dvorkin, J.: Rock-physics diagnostics of depositional texture,
752 diagenetic alterations, and reservoir heterogeneity in high-porosity siliciclastic sediments and rocks — A
753 review of selected models and suggested work flows, Geophysics, 75(5), 75A31-75A47, 2010.

755 Babuška, V. (1968). Elastic anisotropy of igneous and metamorphic rocks. *Studia Geophysica et*
756 *Geodaetica*, *12*(3), 291-303. https://doi.org/10.1007/BF02592385

758 Barruol, G., Bonnin, M., Pedersen, H. Bokelmann, G.H.R. and Tiberi, C.: Belt-parallel mantle flow beneath
759 a halted continental collision: The Western Alps, Earth and Planetary Science Letters, 302, 3–4, 429-438,
760 2011.

762 Barruol, G., Deschamps, A. and Coutant, O.: Mapping upper mantle anisotropy beneath SE France by SKS
763 splitting indicates Neogene asthenospheric flow induced by Apenninic slab roll-back and deflected by the
764 deep Alpine roots, Tectonophysics, 394, 1–2, 125-138, 2004.

766 Barruol, G., and Kern, H.: Seismic anisotropy and shear-wave splitting in lower-crustal and upper-mantle
767 rocks from the Ivrea Zone—Experimental and calculated data, Phys. Earth Planet. Inter. 95, 3-4, 175–194,
768 1996.
769
770 Bascou, J., G. Barruol, A. Vauchez, D. Mainprice, and M. Egydio-Silva: EBSD-measured lattice-preferred
771 orientations and seismic properties of eclogites, Tectonophysics, 342, 61–80, 2001.
772
773 Bayuk, I.O., Ammerman, M., and Chesnokov, E.M.: Upscaling of elastic properties of anisotropic
774 sedimentary rocks, Geophys. J. Int., 172, 842-860, 2008.
775
776 Ben Ismail, W. and D. Mainprice: An olivine fabric database: an overview of upper mantle fabrics and
777 seismic anisotropy, Tectonophysics, 296, 145-157, 1998.
778
779 Berryman, J.G.: Long-wavelength propagation in composite elastic media I. Spherical inclusions, Journal of
780 Acoustical Society of America, 68, 1809-1819, 1980.
781
782 Bezacier, L., Reynard, B., Bass, J.D., Wang, J., and Mainprice, D.: Elasticity of glaucophane, seismic velocities
783 and anisotropy of the subducted oceanic crust, Tectonophysics 494, 201–210, 2010.
784 Bhagat, S.S., Bass, J.D., Smyth, and J.R.: Single-crystal elastic properties of omphacite-C2/C by Brillouin
785 spectroscopy, J. Geophys. Res. Solid Earth 97, 6843–6848, 1992.
786
787 Brown, J.M., Abramson, E.H., and Angel, R.J: Triclinic elastic constants for low albite, Phys. Chem. Miner.
788 33, 256–265, 2006.
789
790 Burlini, L., and Kunze, K.: Fabric and Seismic Properties of Carrara Marble Mylonite, Phys. Chem. Earth, 25,
791 2, 133-139, 2000.
792
793 Challandes, N., Marquer, D., and Villa, I.M.: P-T-t modelling, fluid circulation, and 39Ar-40Ar and Rb-Sr mica
794 ages in the Aar Massif shear zones (Swiss Alps), Swiss J. Geisci., 101, 269-288, 2008.
795
796 Christensen, N.I. Compressional wave velocities in possible mantle rocks to pressures of 30 kilobars, J.
797 Geophys. Res., 79(2), 407-412, 1974.
798
799 Christoffel, E.B.: Über die Fortpflanzung von Stössen durch elastische, feste Körper, Annali di Matematica
800 8, 193–243, 1877.
801
802 Dale, J., Holland, T.B.J.: Geothermobarometry, P–T paths and metamorphic field gradients of high-pressure
803 rocks from the Adula Nappe, Central Alps. Journal of metamorphic Geology, 21, 813-829, 2003.
804
805 Dandekar, D.P.: Variation in the elastic constants of calcite with pressure, Am. Geophys. Union Trans. 49,
806 323 pp., 1968.
807

808   Erdman, M. E., Hacker, B.R., Zandt, G., and Seward, G.: Seismic anisotropy of the crust: Electron-
809   backscatter diffraction measurements from the Basin and Range, Geophys. J. Int., doi:10.1093/gji/ggt287,
810   2013.
811
812   Fry, B., Deschamps, F., Kissling, E., Stehly, L., and Giardini, D.: Layered azimuthal anisotropy of Rayleigh
813   wave phase velocities in the European Alpine lithosphere inferred from ambient noise, Earth Planet. Sci.
814   Lett, 297, 1–2, 95-102, 2010.
815
816   Goncalves, P., Oliot, E., Marquer, D., and Connolly, J.: Role of chemical processes on shear zone formation:
817   an example from the Grimsel metagranodiorite (Aar massif, Central Alps), Journal of Metamorphic
818   Geology. 30. 10.1111/j.1525-1314.2012.00991.x, 2012.
819
820   Hadley, K.: Comparison of calculated and observed crack densities and seismic velocities in Westerly
821   granite. J. Geophys. Res., 81(20), 3484-3494, 1976.
822
823   Hartmann G. and Wedepohl K.H.: The composition of peridotite tectonites from the Ivrea Complex,
824   northern Italy: Residues from melt extraction. Geochim. Cosmochim. Ac., 57, 1761-1782, 1993.
825
826   Heinrich, C. A.: Eclogite facies regional metamorphism of hydrous mafic rocks in the Central
827   Alpine Adula nappe. J. Petrol., 27, 123–154, 1986.
828
829   Hetényi, G. Plomerová, J. Bianchi, I. Kampfová Exnerová, H. Bokelmann, G., Handy, M.R., and Babuška, V.:
830   From mountain summits to roots: crustal structure of the Eastern Alps and Bohemian Massif along
831   longitude 13.3° E, Tectonophysics, 744, 239-255, 2018.
832
833   Heyliger, P., Ledbetter, H., Kim, S.: Elastic constants of natural quartz, J. Acoust. Soc. Am. 114, 644–650,
834   2003.
835
836   Huang, J., Devoe, M., Gomez-Barreiro, J., Ren, Y., Vasin, R., Wenk, H.-R.: Preferred orientation and
837   anisotropy of Slates from Northern Spain. International Journal of Earth Sciences, 2021. (submitted)
838
839   Humbert, P., and Plique, F.: Propriétés élastiques de carbonates rhombohédriques monocristallins calcite,
840   magnésite, dolomite, C.R. Acad. Sci. Paris, 275, 391–394, 1972.
841
842   Ivankina, T.I., Kern, H., and Nikitin, A.N.: Directional dependence of P- and S-wave propagation and
843   polarization in foliated rocks from the Kola superdeep well: evidence from laboratory measurements and
844   calculations based on TOF neutron diffraction, Tectonophysics 407, 25–42, 2005.
845
846   Ivankina, T.I., Zel, I.Yu., Lokajicek, T., Kern, H., Lobanov, K.V., and Zharikov, A.V.: Elastic anisotropy of
847   layered rocks: ultrasonic measurements of plagioclase-biotite-muscovite (sillimanite) gneiss versus
848   texture-based theoretical predictions (effective media modeling), Tectonophysics
849   DOI:10.1016/j.tecto.2017.05.005, 2017.

850

851   Kachanov, M., and Mishakin, V.V.: On crack density, crack porosity, and the possibility to interrelate them,
852   International Journal of Engineering Science, 142, 185-189, 2019.

853

854   Kelly, C. M., D. R. Faulkner, and A. Rietbrock: Seismically invisible fault zones: Laboratory insights into
855   imaging faults in anisotropic rocks, Geophys. Res. Lett., 44, 8205–8212, 2017.

856

857   Keppler, R., Behrmann, J.H., Stipp, M.: Textures of eclogites and blueschists from Syros island, Greece:
858   inferences for elastic anisotropy of subducted oceanic crust, Geophys. Res. Solid Earth
859   DOI:10.1002/2017JB014181, 2017.

860

861   Keppler, R., K. Ullemeyer, J. H. Behrmann, and M. Stipp: Potential of full pattern fit methods for the texture
862   analysis of geological materials: Implications from texture measurements at the recently upgraded
863   neutron time-of-flight diffractometer SKAT, J. Appl. Crystallogr., 47, 1520–1535, 2014.

864

865   Keppler, R., K. Ullemeyer, J. H. Behrmann, M. Stipp, R. Kurzawski, and T. Lokajíček: Crystallographic
866   preferred orientations of exhumed subduction channel rocks from the Eclogite zone of the Tauern Window
867   (eastern Alps, Austia), and implications on rock elastic anisotropies at great depths, Tectonophysics, 647,
868   89–104, 2015.

869

870   Kern, H., Ivankina, T.I., Nikitin, A.N., Lokajicek, T., and Pros, Z.: The effect of oriented microcracks and
871   crystallographic and shape preferred orientation on bulk elastic anisotropy of a foliated biotite gneiss from
872   Outokumpu, Tectonophysics 457, 143–149, 2008.

873

874   Kern, H., & Wenk, H.-R. (1990). Fabric-related velocity anisotropy and shear wave splitting in rocks from
875   the Santa Rosa mylonite zone, California. *Journal of Geophysical Research*, *95*, 11213–11223.
876   https://doi.org/10.1029/JB095iB07p11213

877

878   Kitamura, K.: Constraint of lattice-preferred orientation (LPO) on Vp anisotropy of amphibole-rich rocks,
879   Geophys. J. Intern. 165, 3, 1058-1065, 2006.

880

881   Kossak-Glowczewski, J., Froitzheim, N., Nagel, T.J., Pleuger, J., Keppler, R., Leiss, B., Regent, V.: Along-strike
882   shear-sense reversal in the Vals-Scaradra Shear Zone at the front of the Adula Nappe (Central Alps,
883   Switzerland). Swiss Journal of Geosciences, 110, 677-697, 2017.

884

885   Laubscher, H.P.: Large-scale, thin-skinned thrusting in the southern Alps: Kinematic models, GSA Bull. 96,
886   710-718, 1985.

887

888   Llana-Fúnez, S., and Brown, D.: Contribution of crystallographic preferred orientation to seismic anisotropy
889   across a surface analog of the continental Moho at Cabo Ortegal, Spain. GSA Bull. 124, 9/10, 1495–1513,
890   2012.

891

892   Llana-Fúnez, S., Brown, D., Carbonell, R., Álvarez-Marrón, J., and Salisbury, M.: Seismic anisotropy of upper
893   mantle-lower continental crust rocks in Cabo Ortegal (NW Spain) from crystallographic preferred
894   orientation (CPO) patterns, Trabajos de Geología, Universidad de Oviedo, 29, 432-436, 2009.

896   Lokajicek, T., Kern, H., Svitek, T., and Ivankina, T.: 3D velocity distribution of P- and S-waves in a biotite
897   gneiss, measured in oil as the pressure medium: Comparison with velocity measurements in a multi-anvil
898   pressure apparatus and with texture-based calculated data, Phys. Earth Planet. Inter, 231, 1-15, 2014.

900   Lokajíček, T., Vasin, R., Svitek, T., Petružálek, M., Kotrlý, M., Turková, I., Onysko, R., Wenk, H.R.: Intrinsic
901   elastic anisotropy of Westerly granite observed by ultrasound measurements, microstructural
902   investigations, and neutron diffraction, J. Geophys. Res. Solid Earth, 126, e2020JB020878, 2021.

904   Löw, S: Die tektono-metamorphe Entwicklung der Nördlichen Adula-Decke. Beiträge zur Geologischen
905   Karte der Schweiz N.F., 161, 1–84, 1987.

907   Lüschen, E., B. Lammerer, H. Gebrande, K. Millahn, and TRANSALP Working Group: Orogenic structure of
908   the Eastern Alps, Europe, from TRANSALP deep seismic reflection profiling, Tectonophys., 388 (1-4), 85-
909   102, 2004.

911   Lutterotti, L., Matthies, S., Wenk, H.-R., Schultz, A.J., and Richardson, J.W.: Combined texture and structure
912   analysis of deformed limestone from time-of-flight neutron diffraction spectra, J. Appl. Phys. 81, 594–600,
913   1997.

915   Mainprice, D., Barruol, G. and Ben Ismaïl, W.: The seismic anisotropy of the Earth's mantle: from single
916   crystal to polycrystal. In: Karato, S.-I., Forte, A.M., Liebermann, R.C., Masters, G., Stixrude, L. (Eds.), Earth's
917   deep interior: mineral physics and seismic tomography: from atomic to global: AGU Geophysics
918   Monograph, 237–264, 2000.

920   Mainprice, D., and Humbert, M.: Methods of calculating petrophysical properties from lattice preferred
921   orientation data, Surv. Geophys. 15, 575–592, 1994.

923   Matthies, S.: On the combination of self-consistent and geometric mean elements for the calculation of
924   the elastic properties of textured multi-phase samples, Solid State Phenom., 160, 87–93, 2010.

926   Matthies, S.: GEO-MIX-SELF calculations of the elastic properties of a textured graphite sample at different
927   hydrostatic pressures, J. appl. Crystallogr., 45, 1–16, 2012.

929   Matthies, S., and Humbert, M.: On the principle of a geometric mean of even-rank symmetric tensors for
930   textured polycrystals, J. Appl. Crystallogr. 28, 254–266, 1995.

932   Matthies, S., Lutteroti, and L.,Wenk, H.R.: Advances in Texture Analysis from Diffraction Spectra, J. Appl.
933   Cryst. 30, 31–42, 1997.

934

935 Matthies, S., and Wenk, H.-R.: Transformations for monoclinic crystal symmetry in texture analysis, J. Appl.
936 Cryst., 42, 564-571, 2009.

937

938 Mauler, A., L. Burlini, K. Kunze, P. Philippot, and J.-P. Burg: P-wave anisotropy in eclogites and relationship
939 to the omphacite crystallographic fabric, Phys. Chem. Earth, 15, 119–126, 2000.

940

941 Meyre, C., and Pusching, A. R.: High-pressure metamorphism and deformation at Trescolmen,
942 Adula nappe, Central Alps. Schweizerische Mineralogische und Petrographische Mitteilungen, 73,
943 277–283, 1993.

944

945 Meyre, C., De Capitani, C., and Partsch, J. H.: A ternary solid solution model for omphacite and its
946 application to geothermobarometry of eclogites from the Middle Adula nappe (Central Alps, Switzerland).
947 Journal of Metamorphic Geology, 15, 687–700, 1997.

948

949 Millahn, K., Lüschen, E., Gebrande, H., and TRANSALP Working Group: TRANSALP-cross-line recording
950 during the seismic reflection transect in the Eastern Alps. Tectonophys., 414, 39–49, 2005.

951

952 Molinari I., Obermann A., Kissling E., Hetényi G., Boschi L., and AlpArray-EASI working group: 3D crustal
953 structure of the Eastern Alpine region from ambient noise tomography, Results in Geophysical Sciences,
954 1–4, DOI: 10.1016/j.ringps.2020.100006, 2020.

955

956 Morris, P.R. Elastic constants of polycrystals, Int. J. Eng. Sci., 8,49–61, 1970.

957

958 Nagel, T.J.: Subduction, collision and exhumation recorded in the Adula nappe, central Alps. In:
959 Siegesmund, S., Fügenschuh, B., Froitzheim, N. (Eds.), Tectonic Aspects of the Alpine–Dinarides–
960 Carpathian System: Geological Society, London, Special Publications, 298, 365–392, 2008.

961

962 Nagel, T., De Capitani C. and Frey, M.: Isograds and P-T evolution in the eastern Lepontine Alps
963 (Graubunden, Switzerland). Journal of Metamorphic Geology 20, 309-324, 2002.

964

965 Nishizawa, O. and Yoshino, T.: Seismic velocity anisotropy in mica-rich rocks: an inclusion model,
966 Geophysical Journal International 145, 19-32, 2001.

967

968 Oliot, E., Goncalves, P., and Marquer, D.: Role of plagioclase and reaction softening in a metagranite shear
969 zone at mid-crustal conditions (Gotthard Massif, Swiss Central Alps), J. metamorphic Geol., 28, 849-871,
970 2010.

971

972 Park, M., and Jung H.: Analysis of electron backscattered diffraction (EBSD) mapping of geological
973 materials: precautions for reliably collecting and interpreting data on petro-fabric and seismic anisotropy,
974 Geoscience Journal, DOI: 10.1007/s12303-020-0002-2, 2020.

975

976 Pfiffner, O.A., Frei, W., Finckh, P., and Valasek, P.: Deep seismic reflection profiling in the Swiss Alps:
977 Explosion seismology results for line NFP 20-EAST, Geology, 16, 987-990, 1988.
978
979 Pleuger, J., Hundenborn, R. Kremer, K. Babinka, S. Kurz, W. Jansen, E. and Froitzheim, N.: Structural
980 evolution of Adula nappe, Misox zone, and Tambo nappe in the San Bernardino area: Constraints for the
981 exhumation of the Adula eclogites. Mitteilungen der Österreichischen Geologischen Gesellschaft, 94, 99–
982 122, 2003.
983
984 Pros, Z., Lokajíček, T., Přikryl, R., and Klima, K.: Direct measurement of 3D elastic anisotropy on rocks from
985 the Ivrea Zone (Southern Alps, NW Italy), Tectonophysics 370, 31–47, 2003.
986
987 Punturo, R., Kern, H., Cirrincione, R., Mazzoleni, P., and Pezzino, A.: P- and S-wave velocities and densities
988 in silicate and calcite rocks from the Peloritani mountains, Sicily (Italy): the effect of pressure, temperature
989 and the direction of wave propagation, Tectonophysics 409, 55–72, 2005.
990
991 Reuss A. Berechnung der Fließgrenze von Mischkristallen auf Grund der Plastizitätsbedingung für
992 Einkristalle, Z Angewandte Mathematik Mechanik, 9, 49-58, 1929.
993
994 Sayers, C.: Long-wave seismic anisotropy of heterogeneous reservoirs, Geophys. J. Int., 132, 667-673.
995
996 Schaltegger, U.: Unravelling the pre-Mesozoic history of Aar and Gotthard massifs (Central Alps) by isotopc
997 dating – a review, Schweiz. Mineral. Petrogr. Mitt., 74, 41-51, 1994.
998
999 Schmid, S. M., Fügenschuh, B., Kissling, E., and Schuster, R.:Tectonic map and overall architecture of the
1000 Alpine orogeny, Eclogae Geologicae Helvetiae, 97, 93–117, 2004.
1001
1002 Schmid, S. M., and E. Kissling: The arc of the western Alps in the light of geophysical data on deep crustal
1003 structure, Tectonics, 19, 1, 62–85, 2000.
1004
1005 Schmidtke, M. J., Keppler, R., Kossak-Glowczewski, J., Froitzheim, N., and Stipp, M.: Elastic anisotropies of
1006 rocks in a subduction and exhumation setting, Solid Earth, submitted.
1007
1008 Silver, P.G.: Seismic anisotropy beneath the continents: probing the depths of geology. Annual Review,
1009 Earth and Space Science, 24, 385, 1996.
1010
1011 Simancas, J. F., Tahiri, A., Azor, A., González Lodeiro, F. Martínez Poyatos, D., and El Hadi, H.: The tectonic
1012 frame of the Variscan-Alleghanian Orogen in Southern Europe and Northern Africa, Tectonophysics, 398,
1013 181– 198, 2005.
1014
1015 Smith, G.P. and Ekström, G.: A global study of Pn anisotropy beneath continents, Journal of geophysical
1016 Research, 104, 963–980, 1999.
1017

1018   Steck, A.: Une carte des zones de cisaillement ductile desAlpes Central, Eclogae Geologicae Helvetiae, 83,
1019   3, 603-627, 1990.
1020
1021   Ullemeyer, K., Leiss, B., and Stipp, M.: Textures and Microstructures in Peridotites from the Finero Complex
1022   (Ivrea Zone, Alps) and its Influence on the Elastic Rock Properties, Solid State Phenomena 160, 183-188,
1023   2010.
1024
1025   Ullemeyer, K., Lokajíček, T., Vasin, R.N., Keppler, R., and Behrmann, J.H.: Extrapolation of bulk rock elastic
1026   moduli of different rock types to high pressure conditions and comparison with texture-derived elastic
1027   moduli, Phys. Earth Planet. Inter., 275, 32-43, 2018.
1028
1029   Ullemeyer, K., Siegesmund, S., Rasolofosaon, P.N.J., and Behrmann, J.H.: Experimental and texture-derived
1030   P-wave anisotropy of principal rocks from the TRANSALP traverse: an aid for the interpretation of seismic
1031   field data, Tectonophysics 414, 97–116, 2006.
1032
1033   Ullemeyer, K., Spalthoff, P., Heinitz, J., Isakov, N. N., Nikitin, A. N., and Weber, K.: The SKAT texture
1034   diffractometer at the pulsed reactor IBR-2 at Dubna: Experimental layout and first measurements. Nuclear
1035   Instruments and Methods of Physical Research, 412, 80–88, 1998.
1036
1037   Vasin, R., Wenk, H.-R., Kanitpanyacharoen, W., Matthies, S., and Wirth, R.: Anisotropy of Kimmeridge
1038   shale, J. Geophys. Res. Solid Earth, 118, 3931–3956, 2013.
1039
1040   Vasin, R.N., Lebensohn, R.A., Matthies, S., Tome, C.N., and Wenk, H.-R.: The influence of grain shape and
1041   volume fraction of sheet silicates on elastic properties of aggregates: biotite platelets in an isotropic
1042   matrix, Geophysics, 79, 433–441, 2014.

1043   Vasin, R.N., Kern, H., Lokajíek, T., Svitek, T., Lehmann, E., Mannes, D.C., Chaouche, M., and Wenk, H.-R.:
1044   Elastic anisotropy of Tambo gneiss from Promontogno, Switzerland: a comparison of crystal orientation
1045   and microstructure-based modelling and experimental measurements, Geophys. J. Int., 209, 1–20, 2017.

1046   Vaughan, M.T., and Guggenheim, S.: Elasticity of muscovite and its relationship to crystal structure, J.
1047   Geophys. Res. 91, 4657–4664, 1986.
1048
1049   Vernik, L.: Seismic petrophysics in quantitative interpretation. Society of Exploration Geophysicists, DOI:
1050   10.1190/1.9781560803256, 2016.
1051
1052   Vilhelm, J., Rudajev, V., Zivor, R., Lokajícek, T., and Pros, Z.: Influence of crack distribution of rocks on P-
1053   wave velocity anisotropy – a laboratory and field scale study, Geophysical Prospecting 58, 1099-1110,
1054   2010.
1055
1056

1057 Voigt W. Theoretische Studien über die Elasticitätsverhältnisse der Krystalle. Dieterichsche Verlags-
1058 Buchhandlung, Göttingen. 1887. 100 pp.
1059
1060 Von Dreele, R.B.: Quantitative texture analysis by rietveld refinement, J. Appl. Cryst. 30, 517–525, 1997.
1061
1062 Walsh, J.B.: The effect of cracks on the compressibility of rock. Journal of Geophysical Research, 70(2),
1063 381-389, 1965.
1064
1065 Wehrens, P., Baumberger, R., Berger, A., and Herwegh, M.: How is strain localized in a meta-granitoid,
1066 mid-crustal basement section? Spatial distribution of deformation in the central Aar massif (Switzerland),
1067 Journal of Structural Geology. 94. 10.1016/j.jsg.2016.11.004, 2016.
1068
1069 Weiss, T., Siegesmund, S., Rabbel, W., Bohlen, T., and Pohl, M.: Seismic Velocities and Anisotropy of the
1070 Lower Continental Crust: A Review, Pure appl. geophys., 156, 97–122, 1999.
1071
1072 Wenk, H.-R., Lutterotti, L., and Vogel, S.C.: Rietveld texture analysis from TOF neutron diffraction data,
1073 Powder Diffraction 25, 283–296, 2010.
1074
1075 Wenk, H.-R., Yu, R., Vogel, S., and Vasin R. Preferred orientation of quartz in metamorphic rocks from the
1076 Bergell Alps, Minerals 9(5), 277, 2019.
1077
1078 Worthington, J.R., Hacker, B.R., and Zandt, G.: Distinguishing eclogite from peridotite: EBSD-based
1079 calculations of seismic velocitites. Geophys. J. Int. Seism. DOI:10.1093/gji/ggt004, 2013
1080
1081 Yan, Z., R. W. Clayton, and J. Saleeby: Seismic refraction evidence for steep faults cutting highly attenuated
1082 continental basement in the central transverse ranges, California, Geophys. J. Int., 160, 651–666, 2005.
1083
1084 Zappone, A., Fernàndez,M., García-Duenas, V., and Burlini, L.: Laboratorymeasurements of seismic P-wave
1085 velocities on rocks from the Betic chain (southern Iberian Peninsula), Tectonophysics 317, 259–272, 2000.
1086
1087 Zel, I.Yu.,Ivankina, T.I., Levin, D.M., Lokajicek, T.: P-wave ray velocities and the inverse acoustic problem
1088 for anisotropic media. Crystallography Reports 61, 4, 623-629, 2016.
1089
1090 Zertani, S., John, T., Tilmann, F., Motra, H. B., Keppler, R., Andersen, T. B., and Labrousse, L.: Modification
1091 of the seismic properties of subducting continental crust by eclogitization and deformation processes.
1092 Journal of Geophysical Research: Solid Earth. 124, 9731-9754, 2019.
1093
1094 Zertani, S., Vrijmoed, J. C., Tilmann, F., John, T., Andersen, T. B., and Labrousse, L.: P wave anisotropy
1095 caused by partial eclogitiation of descending crust demonstrated by modeling effective petrophysical
1096 properties. Geochemistry, Geophysics, Geosystems. 20, DOI: 10.1029/2019GC008906, 2020.
1097

1098   Zhang J.J., Santosh M., Wang X.X., Guo L., Yang X.G., and Zhang B.: Tectonics of the northern Himalaya
1099   since the India–Asia collision, Gondwana Research, 21, 4, 939–960, 2012.
1100
1101   Zhang, J.F., Wang, Y.F., and Jin, Z.M.: CPO-induced seismic anisotropy in UHP eclogites, Sci China Ser D-
1102   Earth Sci, Vol. 51, No. 1, 11-21, 2008.
1103